JACS
JOURNAL OF THE AMERICAN CHEMICAL SOCIETY

Article

pubs.acs.org/JACS

Site-Specific Internal Motions in GB1 Protein Microcrystals Revealed by 3D $^{2}H-^{13}C-^{13}C$ Solid-State NMR Spectroscopy

Xiangyan Shi and Chad M. Rienstra*

Department of Chemistry, University of Illinois at Urbana−Champaign, 600 South Mathews Avenue, Urbana, Illinois 61801, United States

Supporting Information

ABSTRACT: ^{2}H quadrupolar line shapes deliver rich information about protein dynamics. A newly designed 3D $^{2}H-^{13}C-^{13}C$ solid-state NMR magic angle spinning (MAS) experiment is presented and demonstrated on the microcrystalline β1 immunoglobulin binding domain of protein G (GB1). The implementation of $^{2}H-^{13}C$ adiabatic rotor-echo-short-pulse-irradiation cross-polarization (RESPIRATION CP) ensures the accuracy of the extracted line shapes and provides enhanced sensitivity relative to conventional CP methods. The 3D $^{2}H-^{13}C-^{13}C$ spectrum reveals ^{2}H line shapes for 140 resolved aliphatic deuterium sites. Motional-averaged ^{2}H quadrupolar parameters obtained from the line-shape fitting identify side-chain motions. Restricted side-chain dynamics are observed for a number of polar residues including K13, D22, E27, K31, D36, N37, D46, D47, K50, and E56, which we attribute to the effects of salt bridges and hydrogen bonds. In contrast, we observe significantly enhanced side-chain flexibility for Q2, K4, K10, E15, E19, N35, N40, and E42, due to solvent exposure and low packing density. T11, T16, and T17 side chains exhibit motions with larger amplitudes than other Thr residues due to solvent interactions. The side chains of L5, V54, and V29 are highly rigid because they are packed in the core of the protein. High correlations were demonstrated between GB1 side-chain dynamics and its biological function. Large-amplitude side-chain motions are observed for regions contacting and interacting with immunoglobulin G (IgG). In contrast, rigid side chains are primarily found for residues in the structural core of the protein that are absent from protein binding and interactions.

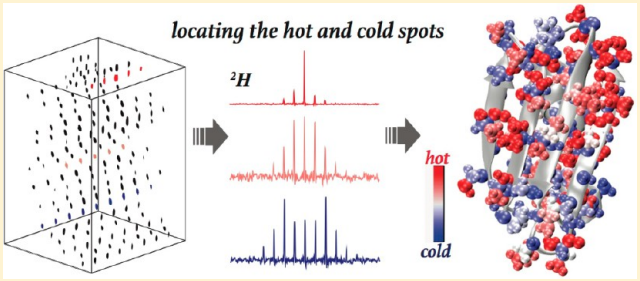

INTRODUCTION

Protein dynamics plays critical roles in biological functions such as enzyme catalysis, ligand binding, and signal transduction.[1,2] It has drawn increasing research attention in recent studies, as protein structures alone do not fully explain biological activities. X-ray diffraction (XRD) and nuclear magnetic resonance (NMR) are the premier methods to determine protein conformation. XRD reports primarily on structure, and the protein flexibility is only indirectly reflected in B-factors. Therefore, it is problematic to address protein dynamics solely from B-factors, which also are affected by crystal packing defects, whole-body motions and refinement artifacts.[3,4] Further, B-factors are insensitive to reorientation motions and are unable to distinguish motions covering different time scales.[3,4] Protein dynamics can be elucidated by NMR[5−11] along with several other techniques, including MD simulations,[12,13] fluorescence spectroscopy,[14,15] and electron paramagnetic resonance (EPR).[16,17] NMR is the premier technique for probing motions in proteins and widely implemented to investigate protein mobility at the atomic level.[5,7,11] Well-developed methods in solution-state NMR include spin relaxation (R_1, R_2, and $R_{1\rho}$),[18−21] Carr−Purcell−Meiboom−Gill (CPMG) relaxation dispersion,[22−24] residual dipolar couplings (RDCs),[25,26] hydrogen−deuterium exchange,[27] and deuterium relaxation.[28] These measurements capture motions with time scales from picoseconds to seconds,[10,11,29−32] which substantially expand our understanding of protein structure and dynamics. For example, a recent study successfully quantified side-chain χ1 distributions by RDCs for the third domain of protein G.[33] Slow molecular tumbling leads to poor spectral resolution and sensitivity, which hinder the application of solution-state NMR to large proteins. In addition, chemical shift anisotropy (CSA), dipolar coupling, and quadrupolar coupling line shapes convey rich information on site-specific motional modes and rates.[7,34−36] These anisotropic interactions are extensively averaged by isotropic Brownian tumbling motions in solution. In contrast, in solid-state NMR, the anisotropic line shapes are retrieved and can be detected accurately to illustrate dynamics of chemical groups in a protein. Similar to solution-state NMR, spin relaxation is routinely implemented in solid-state NMR for investigating dynamics.[7,8,37−40] For example, a recent study determined 13 sets of bulk NMR relaxation times for the β1 immunoglobulin binding domain of protein G (GB1) microcrystals at various temperatures.[41] The results explored the hierarchical distribution of backbone and side-chain motions as well as protein−

Received: December 11, 2015
Published: February 5, 2016

DOI: 10.1021/jacs.5b12974
J. Am. Chem. Soc. 2016, 138, 4105−4119

solvent motion coupling for microcrystalline GB1 over the temperature window of 105−280 K. Recent studies showed that the CPMG relaxation dispersion approach was applicable in the solid state.[42] These solid-state NMR developments paved the way for the elucidation of dynamics in large proteins and especially benefit the study of membrane proteins. Further, high similarity was shown for picosecond to submicrosecond dynamics elucidated by solid-state and solution-state NMR for SH3 and ubiquitin, implying the validation of extrapolating solid-state dynamics information to proteins in their native states.[43−45]

Extensive effort has been devoted to develop solid-state NMR pulse sequences for dynamics detection by utilizing dipole−dipole, CSA, and quadrupolar interactions. For example, studies managed to determine order parameters from scaled $^{1}H-^{13}C$ dipolar couplings measured using homonuclear coupling attenuation pulse schemes such as T-MREV,[46] phase-modulated Lee−Goldberg irradiation,[47] rotational-echo double resonance (REDOR),[48−51] cross polarization combined with phase inversion (CPPI),[52,53] and symmetry-based pulse sequences.[54] Moreover, the use of these dipolar recoupling techniques in solid-state NMR has enabled the elucidation of dynamics for a number of proteins.[55−60] The most commonly used quadrupolar nuclei in biological studies is deuterium, which can be enriched by replacing protons without altering critical chemical and physical properties of the systems. In comparison with the dipolar interaction and CSA, the ^{2}H quadrupolar coupling constant (C_Q) is significantly larger (∼200 kHz), which gives rise to opportunities to study dynamics as well as several spectroscopic challenges. The large amplitude of the ^{2}H C_Q enables much more accurate measurements than those of the dipolar coupling or CSA.[61−65] Currently, however, the ability to quantitatively evaluate protein dynamics is partially complicated by the absence of a complete understanding of rigid-limit quadrupolar tensor values (addressed in the following section). ^{2}H line shape and relaxation time together enable the characterization of protein dynamics covering time scales from picoseconds to seconds.[66−68] On the other hand, limitations of NMR hardware and pulse sequences impede the application of ^{2}H C_Q measurements in large proteins or other macromolecules. Solid-state NMR probes enabling high power irradiation of ^{2}H, simultaneously with ^{1}H and ^{13}C and/or ^{15}N, combined with high magic angle spinning (MAS) rates, allow the efficient excitation and detection of ^{2}H signals in a site-specific fashion with multidimensional NMR. Cross-polarization (CP)[69,70] is one of the most common pulse elements exploited to transfer magnetization in multidimensional solid-state NMR. Several recent studies implemented $^{2}H-^{13}C$ tangent CP transfers in two-/three-dimensional (2D/3D) experiments to indirectly detect ^{2}H quadrupolar line shapes and spin−lattice (T_1) relaxation times to probe dynamics of NAV,[71] amino acids,[72] SH3 protein,[73] and silk proteins.[74,75] As pointed out in previous studies and observed in the current work, conventional $^{2}H-^{13}C$ CP schemes lead to nonuniform magnetization transfer across the broad ^{2}H powder pattern.[72] The optimal CP condition providing accurate ^{2}H line shape covers an extraordinarily narrow rf band (<1 kHz) and is sensitive to ^{2}H C_Q.[72] Thus, it is challenging to measure quadrupolar parameters accurately for sites with different C_Q values using one particular CP condition. This impedes the utilization of conventional $^{2}H-^{13}C$ CP in multidimensional NMR to extract ^{2}H quadrupolar information for proteins as the range of motional averaged C_Q is up to ∼185 kHz.

A recently invented polarization transfer pulse scheme, rotor-echo-short-pulse-irradiation (RESPIRATION) CP,[76−79] shows the potential to overcome the nonuniformity of magnetization transfer observed in conventional CP. This approach provides significantly enhanced efficiency for $^{13}C-^{15}N$, $^{1}H-^{15}N$, as well as $^{2}H-^{13}C$ CP and is more tolerant to the variation of experimental conditions such as rf mismatching, probe detuning, and spinning instability.[78] Later studies demonstrated that adiabatic RESPIRATION CP further improves the performance even using very low rf field strengths.[77,79] These studies primarily focused on the CP efficiency enhancement illustrated by numerical simulations and experimental data. The observed broad $^{2}H-^{13}C$ CP matching profile in adiabatic RESPIRATION CP implies that an optimal CP condition concurrently satisfies chemical groups with different C_Q's, namely, allowing accurate measurement of quadrupolar coupling parameters for all sites in complicated systems like perdeuterated proteins.

In the present work, the adiabatic RESPIRATION CP element is implemented in a 3D $^{2}H-^{13}C-^{13}C$ solid-state NMR experiment to elucidate site-specific protein backbone and side-chain dynamics. We show with crystalline Ala that superior $^{2}H-^{13}C$ magnetization transfer uniformity is observed using adiabatic RESPIRATION CP transfer. SPC-5[80,81] is employed in the 3D experiment to build $^{13}C-^{13}C$ correlations in order to resolve ^{2}H sites. In comparison with commonly used multidimensional experiments that measure $^{1}H-^{13}C/^{15}N$ dipolar coupling constants, the presented 3D $^{2}H-^{13}C-^{13}C$ approach has several advantages for dynamics detection. First, the resulting ^{2}H powder patterns are on the order of 100 kHz, which is significantly larger than $^{1}H-^{13}C/^{15}N$ dipolar spectra covering less than ∼23 kHz. Thus, the current 3D $^{2}H-^{13}C-^{13}C$ method is less prone to measurement error. Second, dipolar measurements have higher demands on experimental conditions including spinning rates and recoupling pulses in order to efficiently suppress homonuclear dipolar couplings and reintroduce heteronuclear dipolar couplings under MAS. In contrast, the 3D $^{2}H-^{13}C-^{13}C$ experiment is more robust because the accuracy of the obtained ^{2}H spectra solely depends on the $^{2}H-^{13}C$ CP step and is ensured by the use of the adiabatic RESPIRATION CP. The third benefit of the 3D $^{2}H-^{13}C-^{13}C$ approach is that it offers improved spectral resolution through using samples which are typically fully deuterated, relative to dipolar measurements requiring protonated samples. However, one drawback to ^{2}H NMR is that the current understanding of rigid-limit C_Q values for proteins is incomplete, consequently impeding the ability to access quantitative dynamics information. Specifically, due to a general lack of systematic studies, the variation of quadrupolar rigid-limit C_Q values for deuterium bonded to sp^3-hybridized carbon has not been fully evaluated for proteins. To assist quantification of protein side-chain motions using ^{2}H relaxation times, two recent solution-state NMR studies indirectly determined the rigid-limit C_Q values for CD_3 in the N-terminal *drk* SH3 domain[82] as well as CαDα in both ubiquitin and GB1 proteins.[83] The methyl deuterium rigid-limit C_Q values were found to be approximately uniform, at 167 ± 1.5 kHz.[82] $^{2}H\alpha$ rigid-limit C_Q values were determined to be 174 kHz on average with 6−8% uncertainty which the authors attribute to possible measurement uncertainties rather than actual C_Q variation.[83] Together, these two studies suggest that the rigid-limit C_Q values for deuterium at methyl and Cα sites in a protein are likely uniform. It is worth noting that the quantification of rigid-limit C_Q values in these studies may be associated with nontrivial

DOI: 10.1021/jacs.5b12974
J. Am. Chem. Soc. 2016, 138, 4105−4119

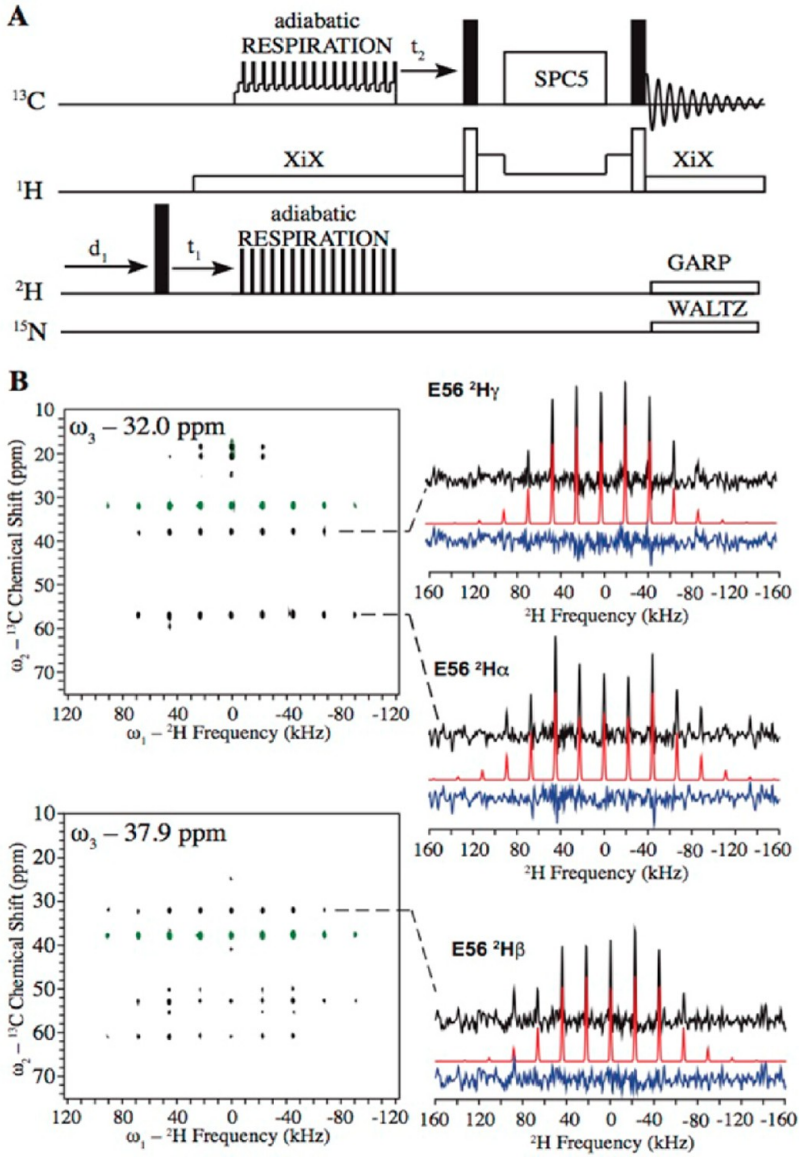

Figure 1. (A) 3D $^{2}H-^{13}C-^{13}C$ solid-state MAS NMR pulse sequence. (B) 2D $^{2}H-^{13}C$ planes of the 3D $^{2}H-^{13}C-^{13}C$ spectrum collected for microcrystalline GB1 and the extracted ^{2}H line shapes for the E56 residue. Experimental line shapes (black), fits (red), and fitting residuals (blue) are displayed in the right column. In the 2D planes, signals with positive and negative intensities are shown in black and green, respectively.

uncertainties resulting from a number of factors.[82,83] To date, the rigid-limit C_Q values for deuterium at sites other than methyl and Cα sites have not been systematically evaluated for proteins. The inherent variation of deuterium quadrupolar interactions in the rigid lattice requires further investigation in order to guide the ^{2}H solution-state and solid-state NMR dynamics studies for proteins. For example, one straightforward approach to obtain the rigid-limit C_Q values is by the measurement of ^{2}H line shapes for proteins with multidimensional MAS solid-state NMR at ultralow temperatures where the motions are quenched, which can be performed with the state-of-the-art NMR instrumentation and is an interesting topic for future studies. In this paper, we focus on the comparison of motionally averaged quadrupolar coupling constant ($\overline{C_Q}$) values for side chains of microcrystalline protein GB1 to gain dynamics information. Because of the lack of the quantitative rigid-limit C_Q values and the complexity brought by the nonzero motional averaged asymmetry parameters ($\overline{\eta}$), we interpret the data by comparing $\overline{C_Q}$ values instead of using generalized order parameters. Such comparisons are performed between the same chemical groups of the same type of residues to minimize uncertainties originating from the potential rigid-limit C_Q differences. This semiquantitative analysis provides critical insights into protein dynamics, especially those of side chains, which have not been systematically studied in detail.

In this study, we demonstrate the 3D $^{2}H-^{13}C-^{13}C$ experiment on microcrystalline GB1, in order to extract ^{2}H quadrupolar information for each chemical group. The obtained $\overline{C_Q}$ and $\overline{\eta}$ elucidate the backbone and side-chain motions for the majority of residues in a site-specific manner. To our knowledge, this is the first example in which the backbone and side-chain dynamic network is fully mapped based on ^{2}H quadrupolar coupling parameters extracted from a single solid-state NMR experiment. The results illustrate that side-chain dynamics of GB1 highly correlate with its structure stability and biological functions. We envisage that this approach will be

DOI: 10.1021/jacs.5b12974
J. Am. Chem. Soc. 2016, 138, 4105–4119

widely applicable to investigate backbone and side-chain motions in various biological systems such as protein microcrystals/nanocrystals, insoluble fibrils, and membrane proteins.

MATERIALS AND METHODS

Preparation of Protein GB1. Uniformly labeled $^{2}H,^{13}C,^{15}N$-GB1 was expressed in *E. coli* BL12(DE3) using a previously published protocol.[84] The protein solution was buffer exchanged against 90/10 D_2O/H_2O to replace 10% of the exchangeable deuterons with protons and then was concentrated to 25 mg/mL and precipitated with 3.0 equiv of 2-methyl-2,4-pentanediol (MPD) and isopropanol (IPA) solution (2:1 MPD/IPA volume ratio).[84] Microcrystalline GB1 was packed into a 1.6 mm standard wall FastMAS rotor (Agilent Technologies Inc.) for use in solid-state NMR experiments.

Solid-State NMR Experiments. Data were collected on a customized 500 MHz Varian VNMRS DirectDrive spectrometer equipped with actively biased transmit−receive circuits and a 1.6 mm FastMAS quadruple resonance $^{1}H-^{13}C-^{2}H-^{15}N$ probe. A 22.222 kHz MAS was chosen as a compromise between peak sensitivity and the number of sidebands present from the ^{2}H manifold. The variable temperature was 0 °C, and the actual sample temperature was 3 °C because of frictional heating induced by MAS (as determined by an ethylene glycol calibration[85]). The 3D $^{2}H-^{13}C-^{13}C$ solid-state NMR pulse sequence is displayed in Figure 1A and will be discussed in detail in the following section. The ^{1}H, ^{13}C, ^{2}H, and ^{15}N $\pi/2$ pulse widths were 1.5, 1.6, 2.9, and 4.5 μs, respectively. In experiments performed on GB1, 86 kHz ^{2}H and 100 kHz ^{13}C spin-lock rf field strengths and a 900 μs contact time were used for adiabatic RESPIRATION CP magnetization transfer. The rotor-synchronized adiabatic RESPIRATION CP waveform was defined by the following optimized parameters: Δ = 4000 rad/s and b = 5000/2π Hz and RESPIRATION pulse τ_p = 1.8 μs (see Jain et al. for parameter definition[79]). The SPC-5 homonuclear recoupling scheme[80,81] was implemented to build $^{13}C-^{13}C$ correlations with a 1.086 ms mixing time. Additional experimental parameters include a 100 ms recycle delay, 400 kHz ^{2}H sweep width, 22.222 kHz and 50 kHz ^{13}C sweep width for the second and third dimension, 192 t_1 increment points, 160 t_2 increment points, and a 20.48 ms acquisition time. Low-power ^{1}H XiX[86] and ^{15}N WALTZ[87] decoupling was employed during the pulse periods as indicated in Figure 1A. Data were processed in nmrPipe[88] and analyzed in Sparky (T. D. Goddard and D. G. Kneller, University of California, San Francisco). ^{2}H MAS line shapes were extracted from the 3D $^{2}H-^{13}C-^{13}C$ correlation experiment and fitted in DMFit.[89]

RESULTS AND DISCUSSION

$^{2}H-^{13}C$ Adiabatic RESPIRATION CP Enabling Accurate Indirect Detection of ^{2}H Line Shapes. Figure 1A shows the 3D $^{2}H-^{13}C-^{13}C$ NMR pulse sequence that was used for detecting ^{2}H quadrupolar line shapes. The initial excited ^{2}H magnetization was transferred to the directly bonded ^{13}C and detected through $^{13}C-^{13}C$ correlation. One critical element is the CP transfer that dictates the accuracy of the extracted ^{2}H line shapes and the sensitivity of the experiment. Conventional tangent CP was previously employed in 2D $^{2}H-^{13}C$ experiments to establish heteronuclear correlation in order to extract ^{2}H line shapes for peptides and proteins.[71−75] One drawback of the approach is that polarization transfer efficiency is not uniform across ^{2}H MAS manifolds.[72] Thus, an optimal CP condition providing accurate ^{2}H line shape is valid only for sites with a particular C_Q. It is unfeasible to use conventional CP to accurately determine ^{2}H line shapes for all sites of a system, particularly in a protein where deuterium C_Q values span ∼185 kHz range. A newly invented polarization transfer scheme, the so-called adiabatic RESPIRATION CP,[77−79] shows the capability to overcome this issue. Motivated by the better performance of this CP scheme over conventional methods, in this section, we focus on evaluating the cross-polarization uniformity that was not previously discussed in detail.

$^{2}H-^{13}C$ adiabatic RESPIRATION CP was first performed on Ala crystalline powder using a pulse sequence displayed in Figure S1A. The rf field strength matching condition profiles were presented in Figure S1B. Polarization efficiency at the optimal condition is enhanced by a factor of 2.4 and 1.8 for Ala methine and methyl groups, respectively, in adiabatic RESPIRATION CP compared with conventional tangent CP. The significantly broader plateau of matching condition observed in the former case illustrates that polarization transfer is less sensitive to CP rf field strength variation (Figure S1B). As shown in a previous study, in a 2D experiment with conventional tangent $^{2}H-^{13}C$ CP, no CP condition provides accurate ^{2}H line shapes for both of the Ala aliphatic groups concurrently.[72] In other words, the CP condition yielding an optimal ^{2}H line shape for one Ala group fails to provide similar CP efficiency for other sites. This arises from the fact that magnetization transfer is nonuniform across the ^{2}H powder pattern in the conventional CP approach. To evaluate the situation in adiabatic RESPIRATION CP, 2D $^{2}H-^{13}C$ correlation experiments were performed with various CP conditions. As presented in Figures S2 and S3, Ala ^{2}H quadrupolar parameters extracted from 2D $^{2}H-^{13}C$ adiabatic RESPIRATION CP experiments remain consistent over a wide range of ^{2}H CP rf carrier frequency offsets. Further, these values agree very well with the quadrupolar parameters obtained from the ^{2}H one-pulse excitation experiment (Figures S2 and S4). Table S1 shows $\overline{C_Q}$ values of Ala $^{2}H\alpha$ and $^{2}H\beta$ extracted from 2D experiments utilizing ^{13}C CP rf field strengths varying between 22 and 77 kHz with the matching ^{2}H rf condition. The differences among the $\overline{C_Q}$ values obtained at various CP conditions are negligible, and the values agree with literature reports for the two Ala aliphatic groups. These results demonstrate that adiabatic RESPIRATION CP fulfills CP transfer uniformity over the ^{2}H powder pattern. Further, it implies that the CP condition providing accurate ^{2}H line shapes is insensitive to rf strengths. This performance is much improved in comparison with tangent CP, where 1 kHz rf strength variation can easily lead to 10% or more $\overline{C_Q}$ difference, as observed in the current work and the previous study.[72] To summarize, utilizing adiabatic RESPIRATION CP for the $^{2}H-^{13}C$ correlation step in multidimensional experiments to indirectly extract ^{2}H line shapes provides the following advantages. First, $^{2}H-^{13}C$ CP efficiency is greatly enhanced. Second, CP transfer is uniform across the ^{2}H powder pattern, ensuring the accuracy of the indirectly extracted ^{2}H line shapes. Third, both CP efficiency and uniformity are much less sensitive to CP condition variation that allows for stable data collection of 3D/4D solid-state NMR spectra. These three features are essential for detecting site-specific deuterium quadrupolar information for proteins possessing deuterium C_Q values typically covering the range of 0 to ∼185 kHz.

3D $^{2}H-^{13}C-^{13}C$ NMR Correlation Experiment Designed for Studying Protein Backbone and Side-Chain Dynamics. A 3D solid-state MAS NMR experiment utilizing adiabatic RESPIRATION CP and SPC-5 homonuclear recoupling to achieve $^{2}H-^{13}C$ and $^{13}C-^{13}C$ correlation, respectively, was designed in order to extract site-specific ^{2}H line shapes for large systems like proteins (Figure 1A). The pulse sequence allows ^{2}H resonances to be resolved with the assistance of $^{13}C-^{13}C$ correlation and the accurate line shapes to

DOI: 10.1021/jacs.5b12974
J. Am. Chem. Soc. 2016, 138, 4105−4119

Table 1. ^{2}H $\overline{C_Q}$ and $\bar{\eta}$ Values Determined for Lys Aliphatic Sites in Microcrystalline GB1[a]

	^{2}Hα		^{2}Hβ		^{2}Hγ		^{2}Hδ		^{2}Hε	
	$\overline{C_Q}$ (kHz)	$\bar{\eta}$	$\overline{C_Q}$ (kHz)	$\bar{\eta}$	$\overline{C_Q}$ (kHz)	$\bar{\eta}$	$\overline{C_Q}$ (kHz)	$\bar{\eta}$	$\overline{C_Q}$ (kHz)	$\bar{\eta}$
K4	160.0 ± 2.1	0.20 ± 0.04	78.6 ± 8.5	0	64.0 ± 2.8	0	50.9 ± 0.4[b]	0	55.5 ± 2.4[b]	0
K10	163.0 ± 3.7	0.25 ± 0.05	103.6 ± 1.2	0.42 ± 0.09	55.3 ± 0.6	0	50.9 ± 0.4[b]	0	55.5 ± 2.4[b]	0
K13	169.1 ± 3.7	0.10 ± 0.09	142.1 ± 3.2	0.02 ± 0.27	116.9 ± 2.7	0.46 ± 0.13	76.9 ± 1.9	0	65.5 ± 1.4	0
K28	157.3 ± 1.6	0.17 ± 0.04	125.4 ± 1.8	0.60 ± 0.05	90.9 ± 1.1	0	74.4 ± 0.7	0	49.0 ± 0.9	0
K31	163.7 ± 2.5	0.10 ± 0.08	141.4 ± 3.5	0.14 ± 0.18	N.D.	N.D.	69.9 ± 2.1	0	70.7 ± 2.6	0
K50	167.7 ± 2.5	0.00 + 0.08	170.2 ± 2.5	0.05 ± 0.07	147.6 ± 1.1	0.17 ± 0.04	136.2 ± 2.1	0.18 ± 0.11	134.6 ± 1.8	0.53 ± 0.04

[a]For deuterium undergoing large-amplitude motion, $\bar{\eta}$ was set to zero for line-shape fitting. [b]The $^{13}C\gamma-^{13}C\delta$ and $^{13}C\delta-^{13}C\xi$ cross peaks of K4 severely overlap with those of K10. The same $^2H\delta$ and $^2H\xi$ quadrupolar values were assigned to K4 and K10, which were obtained from the overlapped ^{2}H line shapes.

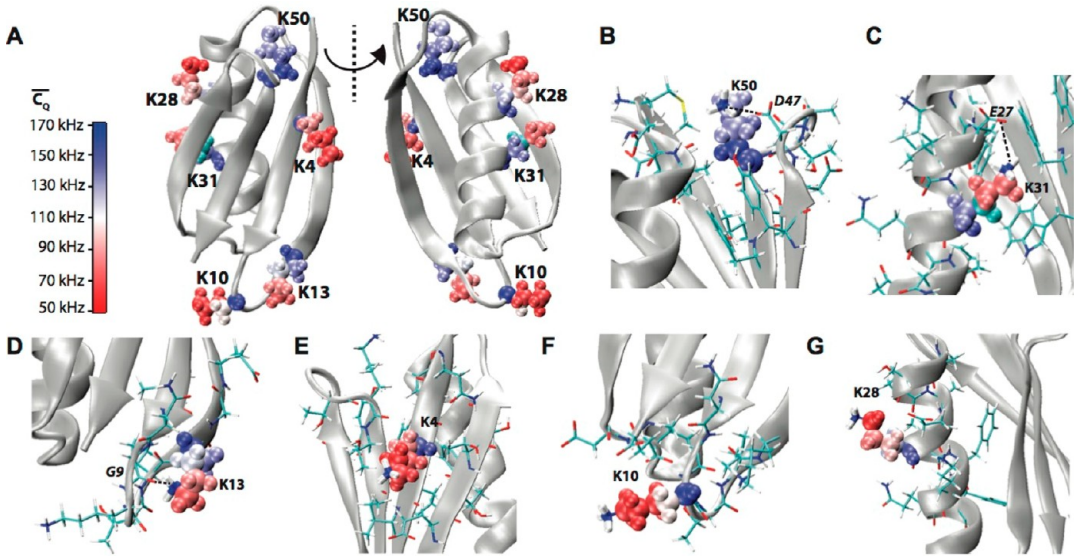

Figure 2. (A) Crystal structure of GB1 (PDB: 2LGI) with Lys aliphatic groups shown in van der Waals spheres and coded with color scaling to $\overline{C_Q}$ values. Two different perspectives are shown for better visualization. (B) K50, (C) K31, (D) K13, (E) K4, (F) K10, and (G) K28 local chemical environment in GB1. The K31 $(CH_2)\beta$ group is color coded with cyan as the $\overline{C_Q}$ value is not determined. The residues having atoms within 5 Å away for the corresponding Lys residue are shown in sticks. The salt bridges between K50 and D47, E27, and K31 and the hydrogen bond between K13 side chain NH_3 and G9 backbone CO are displayed by dash lines.

be extracted from the first indirect dimension. Figure 1B displays 2D planes of the 3D spectrum collected for microcrystalline GB1, where ^{2}H line shapes are extracted for the aliphatic groups of E56. The motional averaged ^{2}H quadrupolar parameters are readily obtained from line-shape fitting. ^{2}H line shapes were extracted from the 3D spectrum for the majority of aliphatic groups, except those subject to resonance overlap or signal absence and aromatic rings exhibiting inefficient CP. Line-shape fitting was performed to extract motional averaged quadrupolar parameters, $\overline{C_Q}$ and $\bar{\eta}$, for 140 chemical groups in GB1, and the fitting results are presented in Figure S5. The obtained ^{2}H quadrupolar parameters convey rich information about protein dynamics that correlate with structure, local chemical environment, salt bridges, hydrogen bonds, and other interactions. To our knowledge, this is the first example that ^{2}H motional averaged quadrupolar parameters have been determined for most sites in a protein. In the following section, discussion will first focus on the side-chain motions and then on the backbone flexibility for microcrystalline GB1.

Lys Side-Chain Dynamics in GB1. ^{2}H line shapes for aliphatic groups of Lys were extracted from the 3D $^2H-^{13}C-^{13}C$ spectrum. Table 1 shows $\overline{C_Q}$ and $\bar{\eta}$ values for Lys aliphatic groups in microcrystalline GB1. The values present a large difference between $^2H\alpha$ and side-chain ^{2}H as well as among Lys residues, indicating various backbone and side-chain motions. $\overline{C_Q}$ and $\bar{\eta}$ contain detailed information about the motional process, requiring analysis on a case-by-case basis depending on the physical property of a chemical group. For example, the line shape of K28 $^2H\beta$ gives a $\overline{C_Q}$ of 125.4 ± 1.8

DOI: 10.1021/jacs.5b12974
J. Am. Chem. Soc. 2016, 138, 4105−4119

kHz and a $\bar{\eta}$ of 0.60 ± 0.05. If a reorientation in the fast-motion regime between two sites with equal population is assumed for the K28 (CH_2) β group, the reorientation angle satisfies $\cos\theta = 0.5$, which is derived from the experimental $\bar{\eta}$. Thus, a $\overline{C_Q}$ of 125.4 kHz corresponds to a C_Q(rigid limit) equal to 200.6 kHz. This large C_Q(rigid-limit) value is physically impossible for a deuteron bonded with an sp^3-hybrized carbon.[64] It infers that the K28 $(CH_2)\beta$ group exhibits more complex dynamics than a simple two-site reorientation, resulting from the combined effect of Cα−Cβ and Cβ−Cγ librations; yet, the motional details involved in this effect are beyond the scope of the current study. Here, the focus is put on the evaluation of the $\overline{C_Q}$ that is proportional to order parameter derived from $\overline{C_Q}/C_Q$(rigid-limit). It is rational to illustrate mobility by comparing $\overline{C_Q}$ values of amino acid aliphatic groups in a protein, even though they do not provide motional details.

The GB1 crystal structure is displayed in Figure 2A with Lys residues shown in van der Waals spheres color coded by $\overline{C_Q}$ values. The observed large $\overline{C_Q}$ variation indicates that molecular dynamics differ significantly among Lys residues in protein GB1. $\overline{C_Q}$ values listed in Table 1 show that the K50 side chain exhibits much more restricted movement than other Lys residues. The flexibility of the amino acid backbone and side chain depends upon the local packing density, salt bridges, hydrogen bonds, and solvent accessibility and can in turn validate these phenomena. The detail of the local structure for K50 is shown in Figure 2B. This residue is in the turn connecting β3 and is exposed to the bulk solvent with more potential for interacting with water molecules (31 water molecules ≤10 Å away from its side chain based upon PDB: 2QMT[90]). It suggests that a very dynamic side chain is expected for K50 that is controversial to the experimental observation. The motion of the K50 side chain is likely restricted by a stable salt bridge formed between K50 $(NH_3)\zeta^+$ and D47 Oγ with a N−O distance of 3.07 Å (PDB: 2QMT[90]). Five out of ten solid-state NMR energy minimum structures (PDB: 2LGI[91]) show that the formation of this salt bridge is allowed where the two groups are 2.73−3.09 Å apart. The existence of a stable salt bridge indicated by the rigid K50 side chain can be used to evaluate the validity of a protein structure model. Similarly, K31 and K13 exhibit moderate side-chain dynamics among the five Lys in GB1, as implied by the $\overline{C_Q}$ values. A salt bridge built between K31 $(NH_3)\zeta^+$ and E27 Oε appears to be the reason for restricted K31 side-chain motion (Figure 2C). The O−N distance is 2.76 Å in the XRD structure (PDB: 2QMT[90]) and ≤4 Å (3.49−3.78 Å) in seven of the ten solid-state NMR minimum energy structures (PDB: 2LGI[91]), allowing the formation of a salt bridge. The $\overline{C_Q}$ values of K13 side-chain deuterium are very similar to those of K31. The solvent-exposure feature of K13 dictates that its side chain likely displays a large degree of mobility (Figure 2D); however, this expectation does not agree with the determined $\overline{C_Q}$ values. Thus, the mobility must be quenched by a salt bridge and/or a hydrogen bond. The local chemical environment suggests that no nearby negatively charged groups are available for forming a salt bridge with K13 side-chain amide group (Figure 2D). Upon the basis of the NMR (PDB: 2LGI[91]) and XRD (PDB: 2QMT[90]) structures, a hydrogen bond is likely formed between K13 $(NH_3)\zeta^+$ and the G9 backbone CO groups with the O−N distance <2.5 Å (2.73 Å in XRD structure) and the O−H−N angle in the range of 122−128°. In addition, the N8 side-chain CO group serves as another potential acceptor for a hydrogen bond formed with K13 $(NH_3)\zeta^+$ as indicated in the XRD structure and one of the ten NMR minimum energy structures. These hydrogen bonds overcome the desolvation energy barrier for K13 and are responsible for rigidifying its side chain. Much more dynamic side chains are observed for K4, K10, and K28. The three residues are completely extended into the solvent and have no neighboring electron acceptors available to form a stable hydrogen bond or a salt bridge (Figure 2E−G). It is noted that a salt bridge could be formed between K4 and E15 side chains based on the distance (3.17 Å) shown in the XRD structure (2QMT[90]). In addition, two intermolecular salt bridges, K4−E42 (4.81 Å) and K10−D40 (4.95 Å), exist in the X-ray crystal structure (2QMT[90]). The presence of these salt bridges seems inconsistent with the large-amplitude side-chain motions observed for K4 and K10. It is likely that the salt bridges are dynamic and are undergoing continual breaking and reformation. Alternatively, it is possible that these salt bridges are absent in the structure of the currently studied GB1 sample, which was prepared with crystallization conditions subtly different from the X-ray study.

Asp and Asn Side-Chain Dynamics in GB1. Motional averaged deuterium quadrupolar coupling constants and asymmetry parameters for Asp and Asn residues are listed in Table 2. Considerable variation is observed for the backbone $^2H\alpha$ and side-chain $^2H\beta$ (Figure 3A). In general, the large $\overline{C_Q}$ values indicate that Asp/Asn local backbones exhibit restricted motions. The side chains are less flexible than those of Lys residues due to the shorter side chains possessing more limited spatial extension. It is shown that the side-chain dynamics are likely further quenched by hydrogen bonds, salt bridges, and desolvation for D22, D36, N37, D46, and D47. As discussed above, D47 $(COO)^-$ forms a stable salt bridge with K50 $(NH_3)\zeta^+$, resulting in the stiffness of side chains for both

Table 2. ^2H $\overline{C_Q}$ and $\bar{\eta}$ Values Determined for Asn and Asp Aliphatic Sites in Microcrystalline GB1 Protein[a]

	$^2H\alpha$		$^2H\beta$	
	$\overline{C_Q}$ (kHz)	$\bar{\eta}$	$\overline{C_Q}$ (kHz)	$\bar{\eta}$
N8	170.7 ± 2.0	0.13 ± 0.05	134.6 ± 6.1	0.47 ± 0.14
D22	142.5 ± 2.5	0.11 ± 0.15	157.6 ± 4.1	0.30 ± 0.06
N35	149.2 ± 2.0	0.20 ± 0.05	88.1 ± 1.3	0
D36	177.0 ± 8.7	0.19 ± 0.11	169.7 ± 3.1	0.18 ± 0.05
N37	161.6 ± 4.6	0.13 ± 0.13	151.2 ± 3.7	0.45 ± 0.05
D40	156.8 ± 2.7	0.01 ± 0.12	123.9 ± 1.5	0.55 ± 0.05
D46	156.2 ± 3.9	0.02 ± 0.16	149.1 ± 3.1	0.33 ± 0.05
D47	156.5 ± 4.6	0.27 ± 0.07	164.4 ± 2.7	0.02 ± 0.11

[a]For deuterium undergoing large-amplitude motion, $\bar{\eta}$ was set to zero for line-shape fitting.

DOI: 10.1021/jacs.5b12974
J. Am. Chem. Soc. 2016, 138, 4105−4119

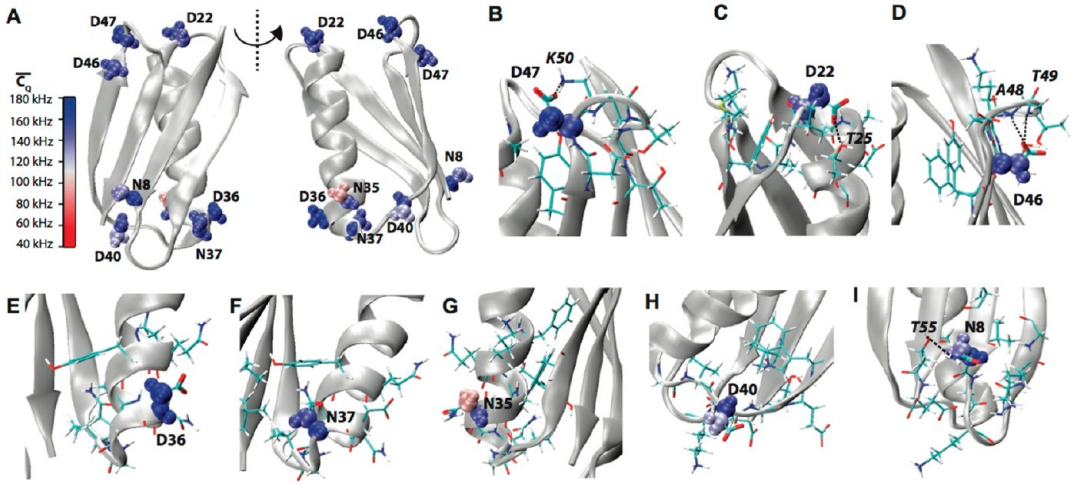

Figure 3. (A) Crystal structure of GB1 (PDB: 2LGI) with Asp and Asn aliphatic groups shown in van der Waals spheres and coded with color scaling to $\overline{C_Q}$ values. Two different perspectives are shown for better visualization. (B) D47, (C) D22, (D) D46, (E) D36, (F) N37, (G) N35, (H) D40, and (I) N8 local chemical environment in GB1. The residues having atoms within 5 Å away for the corresponding Asn or Asp residue are shown in sticks. The salt bridge between D47 and K50 and the hydrogen bonds between D22 and T25, D46 and A48/T49, and N8 and T55 are presented by dashed lines.

residues (Figure 3B). Upon the basis of the chemical environment of D22 (Figure 3C), a strong hydrogen bond likely established between the D22 side chain COO^- group with T25 backbone NH, where the O−N and O−H−N angles are in the range of 1.77−2.02 Å and 138−142°, respectively. Thus, the hydrogen bond contributes to the restricted side-chain motion of D22. Further, it presumes that this strong hydrogen bond formed between the loop and the α helix contributes to the structural stability of GB1. Figure 3D shows the local environment of D46. It infers that the rigid side-chain motion of D46 is due to the hydrogen bonds between COO^- and the A48 backbone NH with an O−N distance of 2.66−2.71 Å and an O−H−N angle of 138−143° according to the solid-state NMR structure (PDB: 2LGI[91]). The T49 NH is another possible electron donor involved in forming a hydrogen bond, which is weaker as the O−N distance is 3.33−3.43 Å and the O−H−N angle is 144−148°. The validity of the hydrogen bonding is further supported by the absence of a competing electron acceptor for D46. It is noted that the O−N distance for the two hydrogen bonds is larger based upon the XRD structure (PDB: 2QMT[90]), 3.11 and 4.13 Å, most likely due to minor structural variation between the solid-state NMR and XRD structures originating from subtle sample preparation differences. The inflexible D36 $(CH_2)\beta$ group is contradictory to its solvent exposure and the lack of hydrogen bonds and a salt bridge (Figure 3E). The possible explanation is that D36 packs close to itself in the crystal lattice, deactivating the side-chain motions. This tight packing is also found to be responsible for its COO^- pK_a value being higher than expected.[92] The $\overline{C_Q}$ values of N37 imply the immobility of the side chain that resides at the edge of the open pocket formed between β strands and the α helix and is partially exposed to solvent (Figure 3F). This unique position does not explain the rigidity of the side chain. It is noted that the Y33 aromatic ring is right above N37 $(NH_2)\delta_2$, allowing the formation of a N−H−π hydrogen bond between the two. Impacted by this hydrogen bond, N37 side-chain motion is significantly restricted. In fact, the N−H−π hydrogen bond is often observed in proteins and greatly contributes to structure stability.[93]

N8, N35, and D40 possess more flexible side chains compared with other Asn and Asp residues discussed above. Among the three, N35 is the most dynamic one as it points outward from the protein surface and interacts with surrounding solvent molecules (Figure 3G). Because of the similar situation, large-amplitude side-chain motion is expected for D40 (Figure 3H). However, it is impacted by an intermolecular interaction, where D40 forms a salt bridge with K10 (4.95 Å).[90,92] As discussed above for K10, the salt bridge, if it exists, is highly dynamic and only slightly rigidifies the D40 and K10 side chains. The N8 side chain presents moderate flexibility due to the coexistence of opposite effects—being mobilized by the surrounding solvent and potentially restricted by hydrogen bonds (Figure 3I). Three out of the ten minimum energy solid-state NMR structures show that a hydrogen bond tends to form between N8 $(NH_2)\delta$ and T55 $(OH)\delta_1$. The O−N distance and O−H−N angle are 2.56−2.59 Å and 141−148°, respectively, according to the NMR structure (PDB: 2LGI[91]). Further, K13 $(NH_3)\zeta^+$ serves as another possible electron donor for hydrogen bonding with the N8 side-chain carbonyl group based upon one of the ten minimum energy solid-state NMR structures (PDB: 2LGI[91]) and the XRD structure (PDB: 2QMT[90]). The validity of these hydrogen bonds is not supported concurrently by the solid-state NMR and XRD structures, which is likely due to minor structural differences originated from the distinct protein crystallization conditions. Despite this, it is rational to conclude at this point that the hydrogen bonds discussed here likely obstruct N8 side chain motions and compensate for the solvent mobilization effect.

Glu and Gln Side-Chain Dynamics in GB1. Table 3 lists motionally averaged deuterium quadrupolar coupling constants and asymmetry parameters for Gln and Glu residues in microcrystalline GB1. The data imply that dynamics vary significantly among these residues, particularly for side chains. Due to the absence of signal, quadrupolar coupling values were not determined for several groups as indicated in Table 3. The absence of signals can happen in one of the three scenarios: inefficient $^2H-^{13}C$ CP transfer, significant ^2H line broadening correlating with $10^{-5}-10^{-6}$ s time scale motion, or zero net $^{13}C-^{13}C$ magnetization transfer during SPC-5 recoupling. The

DOI: 10.1021/jacs.5b12974
J. Am. Chem. Soc. 2016, 138, 4105−4119

Table 3. ^{2}H $\overline{C_Q}$ and $\bar{\eta}$ Values Determined for Glu and Gln Aliphatic Sites in Microcrystalline GB1[a]

	^{2}Hα		^{2}Hβ		^{2}Hγ	
	$\overline{C_Q}$ (kHz)	$\bar{\eta}$	$\overline{C_Q}$ (kHz)	$\bar{\eta}$	$\overline{C_Q}$ (kHz)	$\bar{\eta}$
Q2	155.6 ± 2.5	0.33 ± 0.03	N.D.	N.D.	N.D.	N.D.
E15	155.4 ± 1.8	0.10 ± 0.07	91.5 ± 3.5	0	N.D.	N.D.
E19	168.0 ± 2.7	0.08 ± 0.08	N.D.	N.D.	N.D.	N.D.
E27	169.4 ± 3.3	0.00 + 0.10	158.3 ± 3.3	0.18 ± 0.07	141.4 ± 1.7	0.47 ± 0.03
Q32	164.2 ± 3.5	0.14 ± 0.08	149.4 ± 1.9	0.22 ± 0.05	90.8 ± 2.9	0
E42	165.7 ± 2.3	0.11 ± 0.07	141.1 ± 2.3	0.40 ± 0.05	N.D.	N.D.
E56	160.7 ± 2.5	0.32 ± 0.03	129.0 ± 1.9	0.47 ± 0.05	126.0 ± 1.5	0.47 ± 0.05

[a]For deuterium undergoing large-amplitude motion, $\bar{\eta}$ was set to zero for line-shape fitting.

slow motion in the 10^{-5}–10^{-6} s regime unlikely exists as both the backbone and side chains present $<10^{-7}$ s motion as implied by $\overline{C_Q}$ values measured in this study. Further, efficient ^{13}C–^{13}C polarization transfer is expected for Cβ → Cα as high transfer efficiency is observed in the direction of Cα → Cβ for Q2 and E19. This rules out the third possibility that signal absence is caused by zero net ^{13}C–^{13}C magnetization transfer during the SPC-5 mixing period. Thus, the explanation of signal absence is that ^{2}H–^{13}C cross-polarization is significantly quenched by large-amplitude motion for the groups with undetermined Gln/Glu $\overline{C_Q}$ and $\bar{\eta}$ values.

E27 has the largest $\overline{C_Q}$ values among the seven residues, indicating its rigidity in GB1 microcrystals (Table 3 and Figure 4A). As discussed in the previous section, E27 COO^- forms a salt bridge with K31 $(NH3)\zeta^+$ that significantly hinders side-chain motions for the two residues (Figure 4B). The moderate $\overline{C_Q}$ values (~130 kHz) imply that E56 exhibits restricted side-chain motion that is uncommon for a terminal residue. Figure 4C displays the local chemical environment for E56 in GB1 crystal structure. The side chain points inward to the protein core and places COO^- in a unique position that has a strong tendency to form hydrogen bonds with D40 and the K10 backbone NH. The strong–moderate hydrogen bond between E56 and K10 is expected as the O–H–N angle is close to 180° (162–176°) and the O–N distance is 2.60–3.08 Å according to the solid-state NMR structures (PDB: 2LGI[91]). In addition, a weak hydrogen bond is presumably established between E56 COO^- and K10 considering the values of the O–N distance (3.00–3.49 Å) and the O–H–N angle (119–133°). Thus, E56 side-chain motion is significantly impeded by the two hydrogen bonds. It also explains why strong NMR signals are observed for E56 despite it being the C-terminal residue. Further, the two intrastrand hydrogen bonds likely have great contribution to stabilize the protein structure. The side chain of Q32 is much more dynamic than E27 and E56 illustrated by the $\overline{C_Q}$ values. This is consistent with the local structure, where no hydrogen bond or tight packing is indicated (Figure 4D). Although a relatively large $\overline{C_Q}$ (141.1 kHz) is determined for E42 $(CH_2)\beta$ possibly due to the backbone restriction, its $(CH_2)\gamma$ exhibits larger-amplitude motion in comparison with Glu/Gln (discussed above) as indicated by the undetectable ^{2}H–^{13}C cross-polarization. Thus, E42 $(CH_2)\gamma$ presents large-amplitude mobility because it is solvent exposed and actively interacts with the surrounding water molecules. The significantly motional attenuated $\overline{C_Q}$ (91.5 kHz) is observed for E15 ^{2}Hβ, indicating the side chain is more dynamic than those of E15, E27, Q32, and E56. This is further illustrated by that the mobility of E15 $(CH_2)\gamma$ is significantly enhanced leading to inefficient ^{2}H–^{13}C cross-polarization transfer. The dynamic E15 side chain is consistent with that it points outward from the

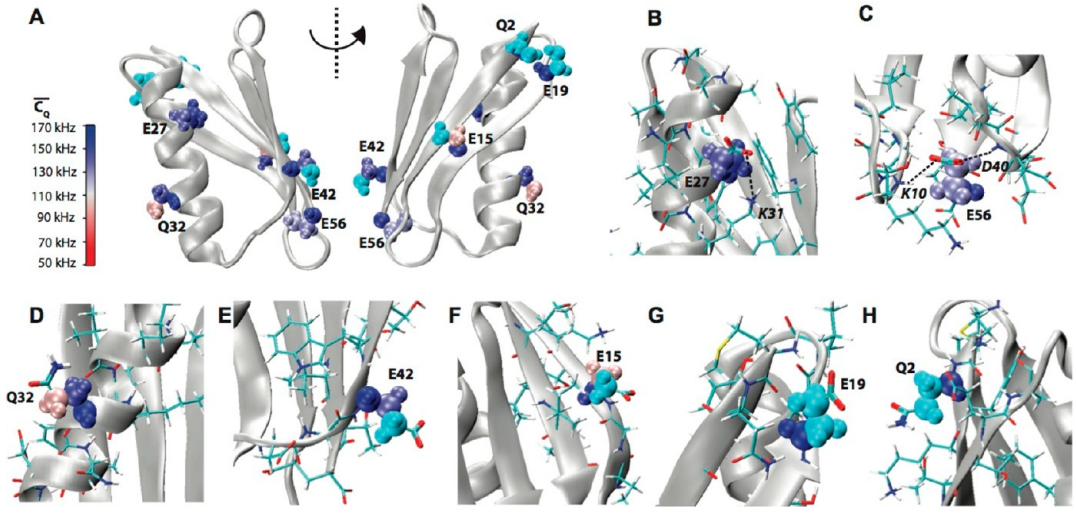

Figure 4. (A) Crystal structure of GB1 (PDB: 2LGI) with Glu and Gln aliphatic groups shown in van der Waals spheres and coded with color scaling to $\overline{C_Q}$ values. Two different perspectives are shown for better visualization. (B) E27, (C) E56, (D) Q32, (E) E42, (F) E15, (G) E19, and (H) Q2 local chemical environment in GB1. Aliphatic groups having deuterium $\overline{C_Q}$ values undetermined are color coded with cyan. The residues having atoms within 5 Å away for the corresponding Glu or Gln residue are shown in sticks. The salt bridge between E27 and K31 and the hydrogen bond between E56 and D40/K10 are presented by dashed lines.

DOI: 10.1021/jacs.5b12974
J. Am. Chem. Soc. 2016, 138, 4105–4119

protein surface and is unlikely to participate in the formation of a hydrogen bond (Figure 4F). However, an intramolecular salt bridge is likely formed between E15 COO^- and K4 $(NH3)\zeta^+$ as supported by the XRD structure (PDB: 2QMT[90]) and E15 pH titration behavior.[92] This seems controversial to the large-amplitude side-chain motions of both E15 and K4. The most likely explanation is that the salt bridge is continually broken and reformed and, therefore, shows negligible impact on the residue side-chain motions. Q2 and E19 possess the most flexible side chains because they are exposed to solvent and have no involvement in any hydrogen bonding or salt bridging (Figure 4G and 4H).

Thr Side-Chain Dynamics in GB1. The side-chain OH group of Thr shows a strong tendency to form a hydrogen bond, particularly with the protein backbone, as it can act as either an electron donor or acceptor.[94,95] The hydrogen bond is expected to impede the dynamics of the Thr side chain to some extent. However, this effect seems to be substantially attenuated based on $\overline{C_Q}$ values determined for Thr residues in microcrystalline GB1. Table 4 lists the motional averaged deuterium quadrupolar coupling parameters for Thr aliphatic groups. It implies that the $(CH_2)\beta$ presents restricted motions as the $\overline{C_Q}$ values are close to those of backbone $^2H\alpha$ for T18, T25, T44, T49, T51, and T55. The difference of $\overline{C_Q}$ is <8 kHz among $(CH_2)\beta$ groups for these residues, illustrating motions with similar amplitudes. Based on the local chemical environment, no hydrogen bond is found for side chain OH groups without ambiguity due to the divergence between reported XRD[90] and NMR[91] structures as well as between different NMR conformers. However, the existence of several hydrogen bonds is expected as supported by NMR conformers and XRD structure. A hydrogen bond likely forms between T55 $(OH)\delta_1$ and N8 $(NH_2)\delta_2$, where the distance of O−N and the angle of O−H−N is 2.56−2.59 Å and 141−148°, respectively, in three of the NMR conformers (Figure 5B). The positions of T25 in five of the lowest energy NMR structures are such that its $(OH)\delta_1$ tends to form a hydrogen bond with a D22 backbone CO group (Figure 5C). The O−O distance and O−H−O angle falls in the range of 3.09−3.10 Å and 159−162°, respectively. As displayed in Figure 5D, T51 has the $(OH)\delta_1$ potentially involved in hydrogen bonding to the T49 backbone NH as shown in the XRD structure (O−O distance is 2.93 Å) and three NMR energy minimum structures (O−N distance and O−H−N angle is 3.15−3.19 Å and 124−141°, respectively). Despite the potential existence of these hydrogen bonds, the $(CH_2)\beta$ groups of the corresponding residues do not show further restricted motions compared to those of T18, T44, and T49.

The motionally reduced C_Q of a Thr $(CH_3)\gamma_2$ originates from two processes—methyl rotation (also considered as three-site reorientation) along its C_{3v} symmetry axis and C_{3v} axis libration. The $\overline{C_Q}$ of a methyl deuterium is equal to 55.67 kHz if assuming a C_Q of 167 ± 1.5 kHz[82] and an ideal tetrahedral geometry for the methyl group and is further reduced by the C_{3v} axis libration. The $(CH_3)\gamma_2$ $\overline{C_Q}$ values of T18, T25, T44, T49, T51, and T55 are all close to this value but exhibit small discrepancies. These deviations could be explained by a slight departure of the methyl group geometry from the ideal tetrahedron. Such methyl geometry distortions have indeed been observed for proteins and small molecules in previous studies.[68,96−98] For example, Ottiger and Bax determined the $H^{methyl}-C^{methyl}-C$ angle deviation for methyl groups of human ubiquitin to be ±1° from 110.9°.[97] In addition, Mittermaier and Kay reported that the angle between the unique axis of the

Table 4. ^2H $\overline{C_Q}$ and $\overline{\eta}$ Values Determined for Thr Aliphatic Sites in Microcrystalline GB1[a]

	$^2H\alpha$		$^2H\beta$		$^2H\gamma_2$	
	$\overline{C_Q}$ (kHz)	$\overline{\eta}$	$\overline{C_Q}$ (kHz)	$\overline{\eta}$	$\overline{C_Q}$ (kHz)	$\overline{\eta}$
T11	152.8 ± 6.9	0.22 ± 0.14	129.7 ± 3.7	0.42 ± 0.11	45.6 ± 0.5	0
T16	157.2 ± 1.4	0.26 ± 0.02	115.7 ± 3.1	0.67 ± 0.12	34.2 ± 1.1	0
T17	152.0 ± 2.0	0.18 ± 0.05	N.D.	N.D.	41.0 ± 0.8	0
T18	158.4 ± 2.4	0.19 ± 0.05	155.2 ± 2.4	0.23 ± 0.05	57.0 ± 0.5	0
T25	165.8 ± 2.6	0.28 ± 0.03	149.5 ± 2.0	0.52 ± 0.03	54.0 ± 0.8	0
T44	172.3 ± 4.3	0.00 + 0.13	149.7 ± 2.2	0.51 ± 0.03	59.8 ± 0.9	0
T49	164.1 ± 2.7	0.30 ± 0.03	148.5 ± 1.7	0.44 ± 0.03	59.1 ± 0.5	0
T51	157.5 ± 2.1	0.24 ± 0.03	152.1 ± 2.7	0.38 ± 0.04	63.6 ± 1.1	0
T53	166.1 ± 6.2	0.19 ± 0.10	N.D.	N.D.	N.D.	N.D.
T55	161.8 ± 2.6	0.27 ± 0.04	146.6 ± 2.3	0.38 ± 0.04	55.2 ± 0.5	0

[a]For deuterium undergoing large-amplitude motion, $\overline{\eta}$ was set to zero for line-shape fitting.

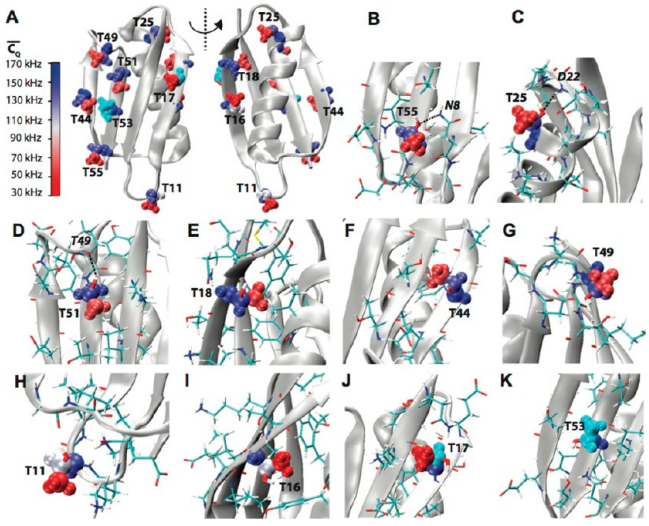

Figure 5. (A) Crystal structure of GB1 (PDB: 2LGI) with Thr aliphatic groups shown in van der Waals spheres and coded with color scaling to $\overline{C_Q}$ values. Two different perspectives are shown for better visualization. (B) T55, (C) T25, (D) T49, (E) T18, (F) T44, (G) T49, (H) T11, (I) T16, (J) T17, and (K) T53 local chemical environment in GB1. Aliphatic groups having deuterium $\overline{C_Q}$ values undetermined are color coded with cyan. The residues having atoms within 5 Å away for the corresponding Thr residues are shown in sticks. The hydrogen bonds between T55 and N8, T25 and D22, and T51 and T49 are presented by dashed lines.

DOI: 10.1021/jacs.5b12974
J. Am. Chem. Soc. 2016, 138, 4105−4119

Table 5. ^{2}H $\overline{C_Q}$ and $\bar{\eta}$ Values Determined for Leu and Ile Aliphatic Sites in Microcrystalline GB1[a]

	^{2}Hα		^{2}Hβ		^{2}Hγ		^{2}Hδ$_1$		^{2}Hδ$_2$	
	$\overline{C_Q}$ (kHz)	$\bar{\eta}$	$\overline{C_Q}$ (kHz)	$\bar{\eta}$	$\overline{C_Q}$ (kHz)	$\bar{\eta}$	$\overline{C_Q}$ (kHz)	$\bar{\eta}$	$\overline{C_Q}$ (kHz)	$\bar{\eta}$
L5	156.4 ± 1.9	0.34 ± 0.03	156.1 ± 4.4	0.40 ± 0.05	149.5 ± 1.0	0.26 ± 0.02	61.0 ± 1.6	0	69.8 ± 2.2	0
L7	165.0 ± 1.7	0.16 ± 0.03	149.3 ± 2.4	0.04 ± 0.14	136.0 ± 1.5	0.63 ± 0.03	N.D.	N.D.	59.3 ± 1.5	0
L12	159.9 ± 1.3	0.15 ± 0.03	141.1 ± 1.3	0.34 ± 0.03	141.4 ± 1.6	0.28 ± 0.05	44.5 ± 0.9	0	40.5 ± 0.7	0
	^{2}Hα		^{2}Hβ		^{2}Hγ$_1$		^{2}Hγ$_2$		^{2}Hδ$_1$	
	$\overline{C_Q}$ (kHz)	$\bar{\eta}$	$\overline{C_Q}$ (kHz)	$\bar{\eta}$	$\overline{C_Q}$ (kHz)	$\bar{\eta}$	$\overline{C_Q}$ (kHz)	$\bar{\eta}$	$\overline{C_Q}$ (kHz)	$\bar{\eta}$
I6	159.4 ± 2.7	0.34 ± 0.03	151.1 ± 3.1	0.45 ± 0.04	92.8 ± 4.4	0.76 ± 0.23	54.2 ± 0.5	0	65.5 ± 5.3	0

[a]For deuterium undergoing large-amplitude motion, $\bar{\eta}$ was set to zero for line-shape fitting. Quadrupolar coupling parameters were not determined for L7 $(CH_2)\delta_1$ due to signal overlap.

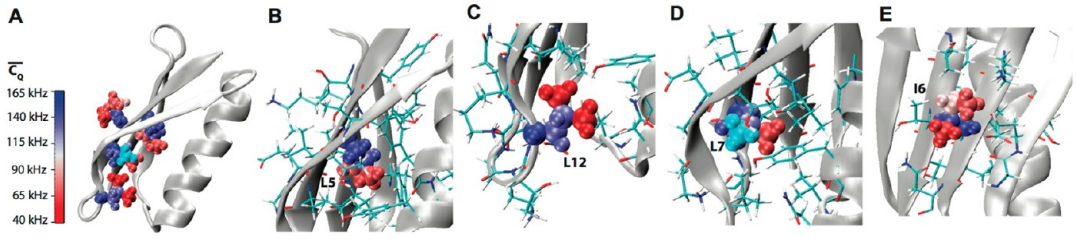

Figure 6. (A) Crystal structure of GB1 (PDB: 2LGI) with Leu and Ile aliphatic groups shown in van der Waals spheres and coded with color scaling to $\overline{C_Q}$ values. (B) L5, (C) L12, (D) L7, and (E) I6 local chemical environment in GB1. Aliphatic groups having deuterium $\overline{C_Q}$ values undetermined are color coded with cyan. The residues having atoms within 5 Å away for the corresponding Leu/Ile residue are shown in sticks.

deuterium electric field gradient tensor and the C_{3v} rotating axis (referred to as β) was 109.5°.[82] It should be noted that the H^{methyl}–C^{methyl}–C angle is not necessary to be identical to the β angle. If a ±1° deviation from 109.5° is assumed for the β angle, a C_Q of 167 ± 1.5 kHz will yield a $\overline{C_Q}$ equaling 53.3–58.8 kHz for a methyl group undergoing fast rotation. The $(CH_3)\gamma_2$ $\overline{C_Q}$ values for T18, T25, T44, T49, and T55 determined here all fall within experimental error of this range, as shown in Table 4. One outlying group is T51 $(CH_3)\gamma_2$, in which the $\overline{C_Q}$ corresponds to its C_{3v} axis departing at least 2.4° from that of the ideal tetrahedral geometry, under the assumption that C_Q is 167 ± 1.5 kHz.[82] Nonetheless, discrepancies of this magnitude are indeed likely to occur in nature, as deviations of 1.9° for the β angle from an ideal tetrahedron have been observed for proteins by previous studies.[96,97] The other possibilities contributing to this large discrepancy include a slight deviation of the actual C_Q from 167 ± 1.5 kHz as well as any unidentified $\overline{C_Q}$ measurement errors. Overall, the six Thr residues exhibit very similar dynamics despite the large variation of local chemical environment; the T18 side-chain points inward to the protein core, while T49 and T44 residues are completely exposed to solvent (Figure 5E–G). It implies that Thr $(CH_2)\beta$ motions are dominantly restricted by the backbone and $(CH_3)\gamma_2$ rotations are in the fast regime and are insensitive to the local geometry as they do not require much free space.

The side chains of T11, T16, and T17 are much more dynamic. $(CH_3)\gamma_2$ $\overline{C_Q}$ values are determined to be less than 46 kHz, which are far smaller than that of a methyl group undergoing three-site reorientation as discussed above. This observation implies the presence of methyl C_{3v} axis librations for these Thr $(CH_3)\gamma_2$ groups. This is typically observed for systems actively interacting with solvent (water) molecules. The local environment indicates that T11, T16, and T17 are fully extended into the solvent (Figure 5H–J). Thus, surrounding solvent significantly mobilizes the side chains of T11, T16, and T17, including the $(CH_2)\beta$ and $(CH_3)\gamma_2$ groups. It is noted that the $\overline{C_Q}$ is not determined for T17 $(CH_2)\beta$ due to weak signal as the ^{2}H–^{13}C cross-polarization transfer is reduced by the large-amplitude motion. Similarly, the absence of NMR signal for T53 $(CH_2)\beta$ and $(CH_3)\gamma_2$ indicates its significant mobile side chain and is consistent with solvent exposure (Figure 5K).

Side-Chain Dynamics of Nonpolar Residues in GB1. In a protein, nonpolar residues are often directed toward the molecule interior, and the side chains have no involvement in strong noncovalent interactions such as hydrogen bonding and salt bridging. The side-chain dynamics are typically dictated by local packing density and solvent accessibility. Here, we discuss the dynamics of the nonpolar residues in GB1 using the determined site-specific deuterium quadrupolar coupling parameters. Motionally averaged $\overline{C_Q}$ and $\bar{\eta}$ values are shown in Table 5 for Leu and Ile residues. It implies that the $(CH_2)\beta$ and $(CH_2)\gamma$ groups in the three residues exhibit motions with similar amplitudes and are dominantly restricted by the rigid backbone. As expected, $(CH_2)\gamma$ groups are slightly more flexible as they extend further away from the backbone. The two $(CH_3)\delta$ groups reside at the end of the side chain and are observed undergoing rotations in the fast motion regime. Again,

DOI: 10.1021/jacs.5b12974
J. Am. Chem. Soc. 2016, 138, 4105–4119

Table 6. ^{2}H $\overline{C_Q}$ and $\bar{\eta}$ Values Determined for Val Aliphatic Sites in Microcrystalline GB1[a]

	^{2}Hα		^{2}Hβ		^{2}Hγ$_1$		^{2}Hγ$_2$	
	$\overline{C_Q}$ (kHz)	$\bar{\eta}$	$\overline{C_Q}$ (kHz)	$\bar{\eta}$	$\overline{C_Q}$ (kHz)	$\bar{\eta}$	$\overline{C_Q}$ (kHz)	$\bar{\eta}$
V21	161.5 ± 1.5	0.13 ± 0.05	N.D.	N.D.	N.D.	N.D.	N.D.	N.D.
V29	159.5 ± 1.7	0.23 ± 0.06	138.5 ± 2.0	0.38 ± 0.05	59.0 ± 2.5	0	51.1 ± 1.5	0
V39	155.2 ± 2.0	0.30 ± 0.03	147.3 ± 3.9	0.41 ± 0.06	57.6 ± 1.3	0	N.D.	N.D.
V54	159.1 ± 3.3	0.42 ± 0.04	149.7 ± 1.5	0.48 ± 0.02	56.7 ± 0.5	0	57.7 ± 0.5	0

[a]For deuterium undergoing large-amplitude motion, $\bar{\eta}$ was set to zero for line-shape fitting.

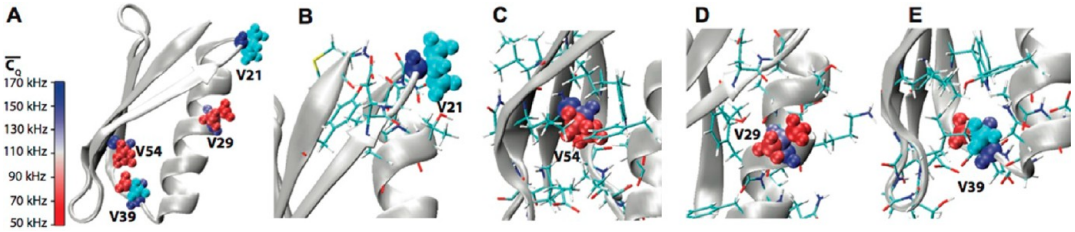

Figure 7. (A) Crystal structure of GB1 (PDB: 2LGI) with Val aliphatic groups shown in van der Waals spheres and coded with color scaling to $\overline{C_Q}$ values. (B) V21, (C) V54, (D) V29, and (E) V39 local chemical environment in GB1. Aliphatic groups having deuterium $\overline{C_Q}$ values undetermined are color coded with cyan. The residues having atoms within 5 Å away for the corresponding Val residue are shown in sticks.

in the current article, we do not focus the subtle differences of $\overline{C_Q}$ and $\bar{\eta}$ that contain detailed dynamics information regarding motional modes. Overall, the deuterium $\overline{C_Q}$ values indicate that the side chain of L5 is the most rigid one among the three. This is attributed to the surrounding high packing density as the side chain is buried deeply in the protein core (Figure 6). The side chain of L12 is more dynamic compared with those of L5 and L7. The $\overline{C_Q}$ values of its two $(CH_3)\delta$ groups are significantly reduced to 40.5 and 44.5 kHz, indicating that the C_{3v} axes of the methyl groups undergo librations, while each deuterium is involved in fast three-site reorientation. The high mobility of the L12 side chain is a consequence of the much lower packing density and partial solvent exposure as displayed in Figure 6C. The moderately crowded local chemical environment of L7 is responsible for the side-chain dynamics with intermediate amplitude between that of L5 and L12 (Figure 6D). As discussed for Thr residues in the previous section, the $\overline{C_Q}$ of a methyl group is reduced to 53.3−58.8 kHz by three-site reorientation if we assume the C_Q equals 167 ± 1.5 kHz[82] and the β angle possesses a 1.0° deviation from 109.5°.[82,97] Thus, the $\overline{C_Q}$ of the L7 $(CH_3)\delta_2$ group (59.3 ± 1.5 kHz) infers the presence of fast methyl group rotation and the immobility of the C_{3v} axis which is equivalent to the rigidity of the Cγ−Cδ_2 bond. In contrast, L5 $(CH_3)\delta$ groups possess $\overline{C_Q}$ values larger than those for methyl groups undergoing free three-site reorientations in the rigid lattice. The $(CH_3)\delta_2$ $\overline{C_Q}$, 61.0 ± 1.6 kHz, exhibits a small discrepancy (within error), possibly due to the methyl geometry departing slightly further from the tetrahedron. The largest discrepancy is observed for the $\overline{C_Q}$ of L5 $(CH_3)\delta_2$, which presents a β angle difference of at least 4.6° relative to an ideal tetrahedral geometry. Such a large deviation has not been reported by any previous study. It is noteworthy that this deviation could simply result from an analytical uncertainty due to the poor signal-to-noise ratio of the L5 $(CH_3)\delta_2$ ^{2}H spectrum (Figure S5), which will require replicated data for error determination. In addition, in the three cases, different $\overline{C_Q}$ values are determined for the two $(CH_2)\delta$ groups. It results from the restricted Cγ−Cδ bond rotation and the distinguishable local pack densities that cause appreciable different effects on the geometries and motions of the two methyl groups. I6 resides in the middle of β1, and the side chain points outward from the protein surface (Figure 6E). I6 $(CH_2)\gamma_1$ possesses a much smaller motional averaged $\overline{C_Q}$ compared with Leu $(CH_2)\gamma$ due to that it is exposed to solvent and less branched. It is interesting to note that the I6 methyl group is not as dynamic as L12 despite the fact that they are both exposed to solvent. This is likely due to the packing density and side-chain geometry differences correlated with the side-chain dihedral angles.

Motional averaged deuterium quadrupolar coupling parameters of Val residues in GB1 are displayed in Table 6. The parameters are not determined for the V21 side chain due to the absence of signal. It indicates that this side chain is significantly mobilized, leading to inefficient ^{2}H → ^{13}C cross-polarization transfer. This is consistent with the local chemical environment in the protein structure, where V21 is in a turn between β2 and the helix and fully extended to the solvent (Figure 7A and B). In contrast, V54 is observed to be the most rigid Val residue in GB1 as indicated by the $\overline{C_Q}$ values. The restricted motion is caused by the high packing density, as this residue points inward and is completely buried in the interior of the protein (Figure 7C). V29 exhibits dynamics with similar amplitudes as V54. The chemical environment shows that V29 resides in the middle of the well-ordered amphipathic helix (Figure 7D). Further, the geometry of the local structure and the short side-chain length

DOI: 10.1021/jacs.5b12974
J. Am. Chem. Soc. 2016, 138, 4105−4119

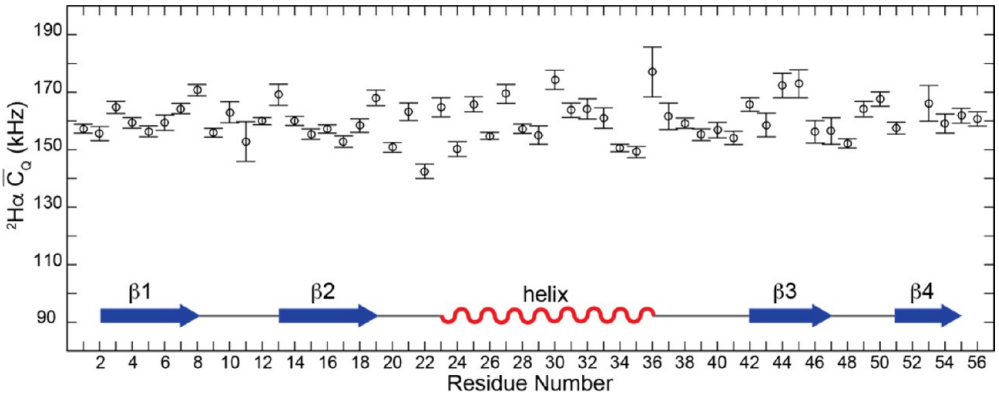

Figure 8. ^{2}Hα $\overline{C_Q}$ values determined for amino acid residues in microcrystalline GB1. The value for residue F52 was not determined due to signal overlap.

likely reduce the possibility of V29 substantially interacting with solvent. V39 is in the loop between β3 and the helix and at the edge of the protein core (Figure 7E). The absence of observable ^{2}H → ^{13}C transfer for V39 $(CH_3)\gamma_2$ implies that the dynamics of this group is significantly enhanced. One possible explanation is that V39 is partially exposed to solvent as shown in Figure 7E, and only $(CH_3)\gamma_2$ actively interacts with solvent due to the restricted Cα−Cβ rotation. The Val dynamics discovered here further explain the polarization transfer efficiency observed for these residues in GB1 in a previous study.[84]

Deuterium quadrupolar coupling parameters were determined for Ala residues in GB1 as listed in Table S2. Despite the large variation in chemical environment, A20, A23, A34, and A48 possess the same ^{2}Hβ $\overline{C_Q}$ value within experimental error (Figure S6). These values agree well with those of methyl groups undergoing fast three-site reorientations in rigid lattices. The small side chain methyl group makes its dynamics much less sensitive to packing density. Slightly larger $\overline{C_Q}$ values are observed for A26 and A24 (Table S3), likely due to similar small deviations from ideal tetrahedral geometry, the discrepancies of the C_Q values, or a combination of the two (as observed for several Thr, Leu, and Ile methyl groups discussed above). It is noted that solvent exposure leads to negligible effect on the dynamics of the Ala side chain. Similarly, weak correlation between dynamics and chemical environment was previously reported for Ala methyl groups in several proteins in solution.[99]

Backbone Dynamics of Microcrystalline GB1. Figure 8 ^{2}Hα shows the $\overline{C_Q}$ values for all residues in microcrystalline GB1 except for F52 of which the $\overline{C_Q}$ is not determined due to signal overlap. It is noted that the ^{2}Hα $\overline{C_Q}$ values are close to those observed for the rigid lattice in peptides and proteins,[71,74,75,100] implying that the backbone in GB1 exhibits high rigidity. Further, the detected nonzero $\overline{\eta}$ values infer that the rigid backbone undergoes small-amplitude fluctuations and reorientations. The overall larger ^{2}Hα $\overline{C_Q}$ values infer that the backbone of GB1 microcrystals exhibits motions with significantly smaller amplitudes in comparison to the side chains. Further, the small variation of the ^{2}Hα $\overline{C_Q}$ indicates the high similarity of local backbone rigidity for all residues in microcrystalline GB1, despite the significant deviations of side-chain motions. This agrees with previous NMR and MD simulation studies showing that the backbone order parameter covers a narrow window.[37,38,83,91,101−103]

If a rigid-limit ^{2}Hα C_Q value of 174 kHz is assumed,[83] the backbone order parameters derived from $\overline{C_Q}$ /C_Q(rigid-limit) cover the range of 0.82−1.0 (Figure S7), which shows a good overall agreement with ^{15}N $R_1/R_{1\rho}$, CαH, and NH dipolar coupling solution-state and solid-state NMR measurements.[37,38,83,91,101−103] Particularly, the backbone order parameters obtained in the present ^{2}H measurements agree very well with previously reported CαHα dipolar coupling data within error on the per residue basis (Figure S7). Somewhat larger discrepancies are observed between the current results and the previous relaxation and NH dipolar coupling data, which likely originates from inherent protein properties and various experimental conditions. First, the CH/CD and NH vectors are motionally distinct from each other, resulting in the discrepancies on the order parameters derived from ^{2}Hα C_Q (or CαH dipolar couplings) and NH dipolar couplings[91] as well as ^{2}Hα and ^{15}N solution-state NMR relaxation rates.[83] Second, discrepancies also exist between CαH vector order parameters derived from the $\overline{C_Q}$ values determined in this work (Figure 4S) and those determined by the previous ^{2}H solution-state NMR relaxation studies.[83] The disagreement could be a consequence of a number of factors, including the non-negligible differences between proteins in solution and microcrystalline forms, experimental temperature differences as well as unidentified systematic uncertainties of the methodologies. Certainly, a quantitative discussion of these disagreements between studies requires complete understanding of these factors; however, this is beyond the scope of the present paper. Overall, the order parameters obtained in the current work fall within the range of 0.82−1.0 and agree well with previous studies. Interestingly, a "zigzag" pattern is observed primarily for the order parameters of the helix regions, which cannot be fully explained by the solvent exposure or packing density. It is noteworthy that the above discussion excludes the motional averaged tensor asymmetry parameters, of which the interpretation is important to characterize details of protein dynamics when using both quadrupolar and dipolar coupling measurements.[104] Slow motions at nanosecond time scales were explored for the GB1 backbone by the solid-state ^{15}N rotating-frame relaxation rate.[37] It is known that the ^{2}H NMR line shapes report the motional modes but not the quantitative motional rates at this dynamic regime, and ^{2}H relaxation measurements are typically employed to assist in elucidating correlation time information.[66,67] Backbone fluctuation/reorientation angles and rates can be extracted from ^{2}H line shapes and relaxation times.

DOI: 10.1021/jacs.5b12974
J. Am. Chem. Soc. 2016, 138, 4105−4119

This type of analysis requires interpretation of $\overline{C_Q}$ and $\overline{\eta}$ with NMR line shape simulations on particular motional models, which is an interesting topic for future studies.

Correlations between the Dynamics of GB1 and Its Structure and Biological Function. In order to understand the side-chain dynamics of GB1 in the context of protein structure and biological function, we map out the side-chain motions across the whole protein as displayed in Figure 9. Chain

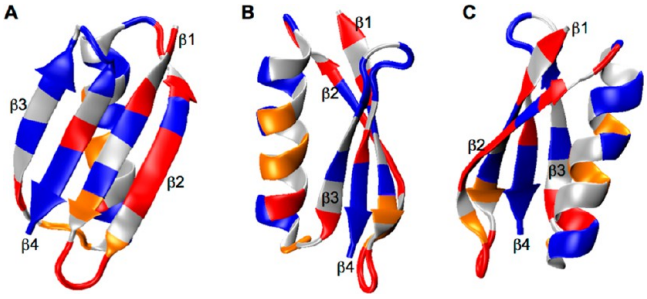

Figure 9. Protein side-chain dynamics map for microcrystalline GB1, shown in three different viewpoints. Lys, Asn, Asp, Gln, Glu, Thr, Leu, and Val residues exhibiting large, moderate, and small amplitude side-chain motions are highlighted in red, orange, and blue, respectively. The rest of the residues (gray) are not considered in this illustration.

lengths, degrees of branching, and polarities have distinct effects on the mobilities of different chemical groups of the side chains. Thus, the side-chain dynamics are identified as large, moderate, and small amplitude motions based on comparisons within the same type of amino acids. The analyses are conducted for amino acids presenting multiple times in GB1, including Lys, Asn/Asp, Gln/Glu, Thr, Leu, and Val, except for Ala residues that exhibit similar dynamics. On the basis of the $\overline{C_Q}$ values, K4, K10, N35, Q2, E15, E19, E42, T11, T16, T17, T53, L12, and V21 exhibit large-amplitude side-chain motions; K13, K28, K31, N8, D40, Q32, and V39 display moderate side-chain flexibilities; K50, D22, D36, N37, D46, D47, T18, T25, T44, T49, T51, T55, L5, L7, V29, and V54 present small-amplitude dynamics. The most dynamic side chains in GB1 are primarily observed for the β2 strand and the loop between the β1 and β2 strands (Figure 9). Previous studies revealed that these domains showed large chemical shift perturbations when binding to immunoglobulin G (IgG) and were involved in interacting with IgG.[105−109] In addition, as shown in Figure 9, side-chain motions with large to moderate amplitudes are present at the helix regions facing the β3 strand and the loop between the helix and the β3 strand, which also serve as binding domains during the interaction with IgG. The overlap between dynamic domains and binding regions suggests that the high degrees of side-chain mobilities play important roles in the contacts and interactions between GB1 and IgG. It is interesting to note that the helix regions facing the opposite direction of the mobile regions (facing way from the β3 strand) possess highly rigid side chains (Figure 9). The corresponding side chains are involved in hydrogen bonding or salt bridging and likely contribute to the stability of the protein structures, while the dynamic regions interact with IgG. The β3 strand serves as another protein binding interface, and the first residue on this β strand, E42, exhibits significant perturbed chemical shifts upon binding IgG.[106] Our results indicate that E42 is highly mobile, which likely contributes to the interaction of GB1 with IgG. It is noteworthy that the remaining residues of the β3 strand demonstrate small-amplitude side-chain motions. Among these, W43 and Y45 have the aromatic rings buried in the core of the protein, leading to the rigidity of side chains that are absent from protein interactions. The other two residues (T44 and D46) also present somewhat restricted side-chain motions. Further, the regions possessing immobile side chains include the β4 strand, the middle portion of the β1 strand, and the loop between the β3 and β4 strands, which are not involved in the interactions with IgG. It is also interesting to note that high flexibility is determined for the side chain of T53 on the β4 strand. Previous studies demonstrated that large chemical shift perturbations occurred to T53 and suggested that this residue might participate in the modulation of hydrogen bonds during protein binding.[108] Thus, the large-amplitude side-chain motions of T53 potentially assist the hydrogen bonding modulation process. In addition, the first several residues on the β1 strand possess flexible side chains as shown in Figure 9, which are expected for terminal regions. Overall, the dynamics of GB1 side chains highly correlate with its biological interactions with IgG. The residues at the binding regions exhibit large-amplitude side-chain motions, which likely facilitate protein contacts and interactions. In contrast, low side-chain mobility is primarily observed for regions that are not involved in protein binding and interactions, and the rigidity of the side chains likely assists in stabilizing the protein structure. These high correlations highlight the importance of side-chain motions in protein activities, which directly correlate to conformational entropy and have critical contributions in energetics of biological events as shown by a number of recent studies.[110−113]

CONCLUSIONS

The study of atomic-level protein dynamics has lagged far behind structure determination due to the lack of high-resolution techniques. The significant role of molecular motions in protein biological function has led to increased demand for developing new approaches to probe molecular dynamics. In the current work, we present a newly designed 3D ^{2}H−^{13}C−^{13}C MAS solid-state NMR pulse sequence. ^{2}H−^{13}C adiabatic RESPRIRATION CP implemented in the 3D pulse sequence allows for the accurate detection of ^{2}H line shapes for deuterium-residing chemical groups in a protein in a site-specific fashion. The extracted motional averaged deuterium quadrupolar parameters provide protein backbone and side-chain dynamics for every isotopically labeled site. Here, ^{2}H line shapes are extracted for 140 chemical groups in the protein from the 3D ^{2}H−^{13}C−^{13}C MAS NMR spectrum collected for microcrystalline GB1. The obtained $\overline{C_Q}$ values elucidate various internal motions exhibited in the protein. The site-specific side-chain dynamics are interpreted by correlating with factors including local structure, packing density, solvent exposure, salt bridging, and hydrogen bonding. It in turn allows for validating the presence of these factors and their impact on protein dynamics and stability. Further, high correlations are demonstrated between GB1 side-chain dynamics and the biological activities. Large-amplitude side-chain motions are observed for regions that are involved in interactions with IgG. In contrast, rigid side chains are primarily found for residues that are in the core of the protein and are absent from protein binding and interactions. It infers that the high mobility of GB1 side chains likely contributes to protein contacts and binding, while the low flexibility of the side chains facilitates maintaining its structures during biological activities. These results provide

DOI: 10.1021/jacs.5b12974
J. Am. Chem. Soc. 2016, 138, 4105−4119

critical insights into the roles of side-chain dynamics in protein biological functions. In perspective, we expect this technique to have wide applications to studies of dynamics for proteins including protein fibrils and microcrystals, as well as large membrane proteins. Further, to date, C_Q has been only systematically reported for ^{2}H at methyl and Cα sites in proteins by solution-state NMR studies.[82,83] The current work is the first study that determines $\overline{C_Q}$ values for the majority of the resolved aliphatic deuterium sites in a protein. These data will enhance and extend the interpretation of ^{2}H relaxation analysis widely used in solution-state and solid-state NMR.

■ ASSOCIATED CONTENT

Supporting Information

The Supporting Information is available free of charge on the ACS Publications website at DOI: 10.1021/jacs.5b12974.

Uniform ^{2}H magnetization transfer in ^{2}H−^{13}C adiabatic RESPIRATION CP (Figures S1, S2, and S3 and Table S1), Ala ^{2}H one-pulse spectrum fit (Figure S4), GB1 ^{2}H line shape fits (Figure S5), Ala dynamics in GB1 (Table S2 and Figure S6), backbone order parameters derived from ^{2}H measurement and CH dipolar measurement (Figure S7), GB1 ^{2}Hα $\overline{\eta}$ values (Figure S8) (PDF)

■ AUTHOR INFORMATION

Corresponding Author

*E-mail: rienstra@illinois.edu.

Notes

The authors declare no competing financial interest.

■ ACKNOWLEDGMENTS

This research is supported by R01-HL103999, R01-GM073770, R01-GM112845, and R21-GM107905. XS is an American Heart Association Postdoctoral Fellow (15POST25700070). We thank Dr. Deborah Berthold for help with GB1 protein sample preparation. We also thank Dr. Kristin Nuzzio, Mr. Dennis Piehl, and Ms. Lisa Della Ripa for careful reading of the manuscript.

■ REFERENCES

(1) Teilum, K.; Olsen, J. G.; Kragelund, B. B. *Cell. Mol. Life Sci.* **2009**, *66*, 2231−2247.
(2) Henzler-Wildman, K.; Kern, D. *Nature* **2007**, *450*, 964−972.
(3) Reichert, D.; Zinkevich, T.; Saalwachter, K.; Krushelnitsky, A. *J. Biomol. Struct. Dyn.* **2012**, *30*, 617−627.
(4) Kuzmanic, A.; Pannu, N. S.; Zagrovic, B. *Nat. Commun.* **2014**, *5*, 3220.
(5) McDermott, A. *Annu. Rev. Biophys.* **2009**, *38*, 385−403.
(6) Meirovitch, E.; Shapiro, Y. E.; Polimeno, A.; Freed, J. H. *Prog. Nucl. Magn. Reson. Spectrosc.* **2010**, *56*, 360−405.
(7) Krushelnitsky, A.; Reichert, D.; Saalwachter, K. *Acc. Chem. Res.* **2013**, *46*, 2028−2036.
(8) Krushelnitsky, A.; Reichert, D. *Prog. Nucl. Magn. Reson. Spectrosc.* **2005**, *47*, 1−25.
(9) Watt, E. D.; Rienstra, C. M. *Anal. Chem.* **2014**, *86*, 58−64.
(10) Kay, L. E. *J. Magn. Reson.* **2005**, *173*, 193−207.
(11) Kleckner, I. R.; Foster, M. P. *Biochim. Biophys. Acta, Proteins Proteomics* **2011**, *1814*, 942−968.
(12) Yang, L. Q.; Sang, P.; Tao, Y.; Fu, Y. X.; Zhang, K. Q.; Xie, Y. H.; Liu, S. Q. *J. Biomol. Struct. Dyn.* **2014**, *32*, 372−393.
(13) Karplus, M.; Kuriyan, J. *Proc. Natl. Acad. Sci. U. S. A.* **2005**, *102*, 6679−6685.
(14) Lam, A. J.; St-Pierre, F.; Gong, Y.; Marshall, J. D.; Cranfill, P. J.; Baird, M. A.; McKeown, M. R.; Wiedenmann, J.; Davidson, M. W.; Schnitzer, M. J.; Tsien, R. Y.; Lin, M. Z. *Nat. Methods* **2012**, *9*, 1005−1012.
(15) Schuler, B. *J. Nanobiotechnol.* **2013**, *11* (Suppl 1), S2.
(16) Nesmelov, Y. E.; Thomas, D. D. *Biophys. Rev.* **2010**, *2*, 91−99.
(17) Fleissner, M. R.; Bridges, M. D.; Brooks, E. K.; Cascio, D.; Kalai, T.; Hideg, K.; Hubbell, W. L. *Proc. Natl. Acad. Sci. U. S. A.* **2011**, *108*, 16241−16246.
(18) Allerhand, A.; Doddrell, D.; Glushko, V.; Cochran, D. W.; Wenkert, E.; Lawson, P. J.; Gurd, F. R. *J. Am. Chem. Soc.* **1971**, *93*, 544−546.
(19) Levy, R. M.; Karplus, M.; Mccammon, J. A. *J. Am. Chem. Soc.* **1981**, *103*, 994−996.
(20) Deverell, C.; Morgan, R. E.; Strange, J. H. *Mol. Phys.* **1970**, *18*, 553−559.
(21) Wittebort, R. J.; Szabo, A. *J. Chem. Phys.* **1978**, *69*, 1722.
(22) Carr, H. Y.; Purcell, E. M. *Phys. Rev.* **1954**, *94*, 630−638.
(23) Luz, Z.; Meiboom, S. *J. Chem. Phys.* **1963**, *39*, 366−370.
(24) Loria, J. P.; Rance, M.; Palmer, A. G. *J. Am. Chem. Soc.* **1999**, *121*, 2331−2332.
(25) Tolman, J. R.; Flanagan, J. M.; Kennedy, M. A.; Prestegard, J. H. *Proc. Natl. Acad. Sci. U. S. A.* **1995**, *92*, 9279−9283.
(26) Saupe, A.; Englert, G. *Phys. Rev. Lett.* **1963**, *11*, 462−464.
(27) Woodward, C. K.; Hilton, B. D. *Annu. Rev. Biophys. Bioeng.* **1979**, *8*, 99−127.
(28) Muhandiram, D. R.; Yamazaki, T.; Sykes, B. D.; Kay, L. E. *J. Am. Chem. Soc.* **1995**, *117*, 11536−11544.
(29) Gobl, C.; Madl, T.; Simon, B.; Sattler, M. *Prog. Nucl. Magn. Reson. Spectrosc.* **2014**, *80*, 26−63.
(30) Mittermaier, A.; Kay, L. E. *Science* **2006**, *312*, 224−228.
(31) Sheppard, D.; Sprangers, R.; Tugarinov, V. *Prog. Nucl. Magn. Reson. Spectrosc.* **2010**, *56*, 1−45.
(32) Göbl, C.; Tjandra, N. *Entropy* **2012**, *14*, 581−598.
(33) Li, F.; Grishaev, A.; Ying, J.; Bax, A. *J. Am. Chem. Soc.* **2015**, *137*, 14798−14811.
(34) Im, W.; Jo, S.; Kim, T. *Biochim. Biophys. Acta, Biomembr.* **2012**, *1818*, 252−262.
(35) Hu, F.; Luo, W.; Hong, M. *Science* **2010**, *330*, 505−508.
(36) Bocian, D. F.; Chan, S. I. *Annu. Rev. Phys. Chem.* **1978**, *29*, 307−335.
(37) Lewandowski, J. R.; Sass, H. J.; Grzesiek, S.; Blackledge, M.; Emsley, L. *J. Am. Chem. Soc.* **2011**, *133*, 16762−16765.
(38) Mollica, L.; Baias, M.; Lewandowski, J. R.; Wylie, B. J.; Sperling, L. J.; Rienstra, C. M.; Emsley, L.; Blackledge, M. *J. Phys. Chem. Lett.* **2012**, *3*, 3657−3662.
(39) Lewandowski, J. R. *Acc. Chem. Res.* **2013**, *46*, 2018−2027.
(40) Krushelnitsky, A.; Zinkevich, T.; Reif, B.; Saalwachter, K. *J. Magn. Reson.* **2014**, *248*, 8−12.
(41) Lewandowski, J. R.; Halse, M. E.; Blackledge, M.; Emsley, L. *Science* **2015**, *348*, 578−581.
(42) Tollinger, M.; Sivertsen, A. C.; Meier, B. H.; Ernst, M.; Schanda, P. *J. Am. Chem. Soc.* **2012**, *134*, 14800−14807.
(43) Agarwal, V.; Xue, Y.; Reif, B.; Skrynnikov, N. R. *J. Am. Chem. Soc.* **2008**, *130*, 16611−16621.
(44) Haller, J. D.; Schanda, P. *J. Biomol. NMR* **2013**, *57*, 263−280.
(45) Chevelkov, V.; Xue, Y.; Linser, R.; Skrynnikov, N. R.; Reif, B. *J. Am. Chem. Soc.* **2010**, *132*, 5015−5017.
(46) Hohwy, M.; Jaroniec, C. P.; Reif, B.; Rienstra, C. M.; Griffin, R. G. *J. Am. Chem. Soc.* **2000**, *122*, 3218−3219.
(47) Vinogradov, E.; Madhu, P. K.; Vega, S. *J. Chem. Phys.* **2001**, *115*, 8983.
(48) Gullion, T.; Schaefer, J. *J. Magn. Reson.* **1989**, *81*, 196−200.
(49) Gullion, T.; Schaefer, J. *Adv. Magn. Opt. Reson.* **1989**, *13*, 57−83.
(50) Jaroniec, C. P.; Tounge, B. A.; Rienstra, C. M.; Herzfeld, J.; Griffin, R. G. *J. Magn. Reson.* **2000**, *146*, 132−139.
(51) Schanda, P.; Meier, B. H.; Ernst, M. *J. Magn. Reson.* **2011**, *210*, 246−259.
(52) Dvinskikh, S. V.; Zimmermann, H.; Maliniak, A.; Sandström, D. *J. Magn. Reson.* **2003**, *164*, 165−170.

DOI: 10.1021/jacs.5b12974
J. Am. Chem. Soc. 2016, 138, 4105−4119

(53) Dvinskikh, S. V.; Zimmermann, H.; Maliniak, A.; Sandstrom, D. *J. Chem. Phys.* **2005**, *122*, 44512.
(54) Levitt, M. H. In *Encyclopedia of Nuclear Magnetic Resonance*; Grant, D. M., Harris, R. K., Eds.; John Wiley & Sons: Chichester U.K., 2002; Vol. *9*, pp 165−196.
(55) Lorieau, J. L.; Day, L. A.; McDermott, A. E. *Proc. Natl. Acad. Sci. U. S. A.* **2008**, *105*, 10366−10371.
(56) Lorieau, J. L.; McDermott, A. E. *J. Am. Chem. Soc.* **2006**, *128*, 11505−11512.
(57) Zhao, X.; Sudmeier, J. L.; Bachovchin, W. W.; Levitt, M. H. *J. Am. Chem. Soc.* **2001**, *123*, 11097−11098.
(58) Schanda, P.; Meier, B. H.; Ernst, M. *J. Am. Chem. Soc.* **2010**, *132*, 15957−15967.
(59) Yang, J.; Tasayco, M. L.; Polenova, T. *J. Am. Chem. Soc.* **2009**, *131*, 13690−13702.
(60) Chevelkov, V.; Fink, U.; Reif, B. *J. Am. Chem. Soc.* **2009**, *131*, 14018−14022.
(61) Meirovitch, E.; Liang, Z.; Freed, J. H. *J. Phys. Chem. B* **2015**, *119*, 2857−2868.
(62) Torchia, D. A. *Annu. Rev. Biophys. Bioeng.* **1984**, *13*, 125−144.
(63) Torchia, D. A.; Szabo, A. *J. Magn. Reson.* **1982**, *49*, 107−121.
(64) Olympia, P. L.; Wei, I. Y.; Fung, B. M. *J. Chem. Phys.* **1969**, *51*, 1610−1614.
(65) Hologne, M.; Chevelkov, V.; Reif, B. *Prog. Nucl. Magn. Reson. Spectrosc.* **2006**, *48*, 211−232.
(66) Jelinski, L. W. *Annu. Rev. Mater. Sci.* **1985**, *15*, 359−377.
(67) Hologne, M.; Hirschinger, J. *Solid State Nucl. Magn. Reson.* **2004**, *26*, 1−10.
(68) Batchelder, L. S.; Niu, C. H.; Torchia, D. A. *J. Am. Chem. Soc.* **1983**, *105*, 2228−2231.
(69) Pines, A.; Gibby, M. G.; Waugh, J. S. *J. Chem. Phys.* **1973**, *59*, 569−590.
(70) Hartmann, S. R.; Hahn, E. L. *Phys. Rev.* **1962**, *128*, 2042−2053.
(71) Hologne, M.; Chen, Z.; Reif, B. *J. Magn. Reson.* **2006**, *179*, 20−28.
(72) Shi, X.; Yarger, J. L.; Holland, G. P. *J. Magn. Reson.* **2013**, *226*, 1−12.
(73) Hologne, M.; Faelber, K.; Diehl, A.; Reif, B. *J. Am. Chem. Soc.* **2005**, *127*, 11208−11209.
(74) Shi, X.; Yarger, J. L.; Holland, G. P. *Chem. Commun.* **2014**, *50*, 4856−4859.
(75) Shi, X.; Holland, G. P.; Yarger, J. L. *Biomacromolecules* **2015**, *16*, 852−859.
(76) Wei, D.; Akbey, U. m.; Paaske, B.; Oschkinat, H.; Reif, B.; Bjerring, M.; Nielsen, N. C. *J. Phys. Chem. Lett.* **2011**, *2*, 1289−1294.
(77) Nielsen, A. B.; Jain, S.; Ernst, M.; Meier, B. H.; Nielsen, N. C. *J. Magn. Reson.* **2013**, *237*, 147−151.
(78) Jain, S.; Bjerring, M.; Nielsen, N. C. *J. Phys. Chem. Lett.* **2012**, *3*, 703−708.
(79) Jain, S. K.; Nielsen, A. B.; Hiller, M.; Handel, L.; Ernst, M.; Oschkinat, H.; Akbey, U.; Nielsen, N. C. *Phys. Chem. Chem. Phys.* **2014**, *16*, 2827−2830.
(80) Hohwy, M.; Rienstra, C. M.; Griffin, R. G. *J. Chem. Phys.* **2002**, *117*, 4973−4987.
(81) Hohwy, M.; Rienstra, C. M.; Jaroniec, C. P.; Griffin, R. G. *J. Chem. Phys.* **1999**, *110*, 7983−7992.
(82) Mittermaier, A.; Kay, L. E. *J. Am. Chem. Soc.* **1999**, *121*, 10608−10613.
(83) Sheppard, D.; Li, D. W.; Bruschweiler, R.; Tugarinov, V. *J. Am. Chem. Soc.* **2009**, *131*, 15853−15865.
(84) Franks, W. T.; Zhou, D. H.; Wylie, B. J.; Money, B. G.; Graesser, D. T.; Frericks, H. L.; Sahota, G.; Rienstra, C. M. *J. Am. Chem. Soc.* **2005**, *127*, 12291−12305.
(85) Van Geet, A. L. *Anal. Chem.* **1968**, *40*, 2227−2229.
(86) Ernst, M.; Samoson, A.; Meier, B. H. *J. Magn. Reson.* **2003**, *163*, 332−339.
(87) Shaka, A. J.; Keeler, J.; Freeman, R. *J. Magn. Reson.* **1983**, *53*, 313−340.
(88) Delaglio, F.; Grzesiek, S.; Vuister, G. W.; Zhu, G.; Pfeifer, J.; Bax, A. *J. Biomol. NMR* **1995**, *6*, 277−293.
(89) Massiot, D.; Fayon, F.; Capron, M.; King, I.; Le Calve, S.; Alonso, B.; Durand, J. O.; Bujoli, B.; Gan, Z. H.; Hoatson, G. *Magn. Reson. Chem.* **2002**, *40*, 70−76.
(90) Schmidt, H. L. F.; Sperling, L. J.; Gao, Y. G.; Wylie, B. J.; Boettcher, J. M.; Wilson, S. R.; Rienstra, C. A. *J. Phys. Chem. B* **2007**, *111*, 14362−14369.
(91) Wylie, B. J.; Sperling, L. J.; Nieuwkoop, A. J.; Franks, W. T.; Oldfield, E.; Rienstra, C. M. *Proc. Natl. Acad. Sci. U. S. A.* **2011**, *108*, 16974−16979.
(92) Schmidt, H. L.; Shah, G. J.; Sperling, L. J.; Rienstra, C. M. *J. Phys. Chem. Lett.* **2010**, *1*, 1623−1628.
(93) Salonen, L. M.; Ellermann, M.; Diederich, F. *Angew. Chem., Int. Ed.* **2011**, *50*, 4808−4842.
(94) Eswar, N.; Ramakrishnan, C. *Protein Eng., Des. Sel.* **2000**, *13*, 227−238.
(95) Vijayakumar, M.; Qian, H.; Zhou, H. X. *Proteins: Struct., Funct., Genet.* **1999**, *34*, 497−507.
(96) Vugmeyster, L.; Ostrovsky, D.; Lipton, A. S. *J. Phys. Chem. B* **2013**, *117*, 6129−6137.
(97) Ottiger, M.; Bax, A. *J. Am. Chem. Soc.* **1999**, *121*, 4690−4695.
(98) Iijima, T.; Tsuchiya, S. *J. Mol. Spectrosc.* **1972**, *44*, 88−107.
(99) Mittermaier, A.; Kay, L. E.; Forman-Kay, J. D. *J. Biomol. NMR* **1999**, *13*, 181−185.
(100) Sarkar, S. K.; Young, P. E.; Torchia, D. A. *J. Am. Chem. Soc.* **1986**, *108*, 6459−6464.
(101) Barchi, J. J., Jr.; Grasberger, B.; Gronenborn, A. M.; Clore, G. M. *Protein Sci.* **1994**, *3*, 15−21.
(102) Seewald, M. J.; Pichumani, K.; Stowell, C.; Tibbals, B. V.; Regan, L.; Stone, M. J. *Protein Sci.* **2000**, *9*, 1177−1193.
(103) Idiyatullin, D.; Nesmelova, I.; Daragan, V. A.; Mayo, K. H. *Protein Sci.* **2003**, *12*, 914−922.
(104) Schanda, P.; Huber, M.; Boisbouvier, J.; Meier, B. H.; Ernst, M. *Angew. Chem., Int. Ed.* **2011**, *50*, 11005−11009.
(105) Derrick, J. P.; Wigley, D. B. *Nature* **1992**, *359*, 752−754.
(106) Gronenborn, A. M.; Clore, G. M. *J. Mol. Biol.* **1993**, *233*, 331−335.
(107) Lian, L. Y.; Barsukov, I. L.; Derrick, J. P.; Roberts, G. C. K. *Nat. Struct. Biol.* **1994**, *1*, 355−357.
(108) Lamley, J. M.; Iuga, D.; Oster, C.; Sass, H. J.; Rogowski, M.; Oss, A.; Past, J.; Reinhold, A.; Grzesiek, S.; Samoson, A.; Lewandowski, J. R. *J. Am. Chem. Soc.* **2014**, *136*, 16800−16806.
(109) Kato, K.; Lian, L. Y.; Barsukov, I. L.; Derrick, J. P.; Kim, H. H.; Tanaka, R.; Yoshino, A.; Shiraishi, M.; Shimada, I.; Arata, Y.; Roberts, G. C. K. *Structure* **1995**, *3*, 79−85.
(110) Wand, A. J. *Curr. Opin. Struct. Biol.* **2013**, *23*, 75−81.
(111) Marlow, M. S.; Dogan, J.; Frederick, K. K.; Valentine, K. G.; Wand, A. J. *Nat. Chem. Biol.* **2010**, *6*, 352−358.
(112) Frederick, K. K.; Marlow, M. S.; Valentine, K. G.; Wand, A. J. *Nature* **2007**, *448*, 325−329.
(113) Lee, A. L.; Wand, A. J. *Nature* **2001**, *411*, 501−504.

DOI: 10.1021/jacs.5b12974
J. Am. Chem. Soc. 2016, 138, 4105−4119